



university of
 groningen

faculty of science
 and engineering

zernike institute for
 advanced materials

DIRECT LASER WRITING OF GRAPHENE ON NICKEL AND PLATINUM

Fika Fauzi

S2684349

A thesis submitted in partial fulfillment of the
 requirements for the degree of

M.Sc. in Physics

University of Groningen

July 2017

Supervisors:

Prof. Dr. M. A. Stöhr (Supervisor I)

Dr. R. I. Tobey (Supervisor II)

N. D. R. Schmidt (Daily Supervisor)

Surface and Thin Film group in collaboration with Optical Condensed Matter Physics group
Zernike Institute for Advanced Materials

ABSTRACT

Direct Laser Writing of Graphene on Nickel and Platinum

Graphene is a promising material for emerging electronic devices with outstanding properties. To integrate graphene into practical circuits for electronic devices, one needs to pattern of graphene. Many methods are developed to pattern graphene, one of which is using laser-assisted chemical vapor deposition.

We built a homemade laser-assisted chemical vapor deposition chamber for direct writing of graphene line. The system has several tunable parameters that influenced the graphene growth on the sample. We did a systematic study of laser-assisted graphene growth on nickel foil. We varied six parameters to obtain the recipe for graphene growth on nickel foil. Those parameters were laser power, beam diameter, scanning rate, gas mixture, base pressure, and foil thickness. The most promising parameters were also adopted to grow graphene on platinum foil.

The laser intensity and foil thickness needed to be tuned to generate growth temperature suitable for graphene growth on nickel foil. By varying the gas mixture and scanning rate under a base pressure of 10^{-7} mbar, we obtained Raman spectra of wrinkled multilayer graphene and of hydrogenated amorphous carbon. These spectra were also found on platinum foil when using a gas mixture of 6×10^{-3} mbar of methane and 1×10^{-3} mbar of hydrogen and a scanning rate of 50 $\mu\text{m/s}$. The scanning electron microscopy was employed to confirm the presence of a wrinkled multilayer graphene on nickel and platinum.

We successfully wrote a line of graphene on both nickel and platinum. Even though the laser-assisted chemical vapor deposition of graphene on nickel foil has been reported, the one on platinum foil has not been reported yet. These findings can provide a rapid fabrication of graphene patterns and open a door for fabricating various graphene-based devices.

Contents

Contents	3
List of Figures.....	5
List of Tables	8
Chapter 1.....	9
Introduction	9
1.1. General Introduction.....	9
1.2. Research Goal	11
1.3. Thesis Structure Overview	12
Chapter 2.....	13
Graphene	13
2.1. The sp^2 Hybridization in Graphene.....	13
2.2. Electronic Band Structure of Graphene.....	15
2.3. Graphene-Metal Interfaces.....	17
Chapter 3.....	22
Characterization and Experimental Techniques	22
3.1. Raman Spectroscopy.....	22
3.2. Scanning Electron Microscopy	24
3.3. Chemical Vapor Deposition	26
3.3. Laser-assisted Chemical Vapor Deposition	28
Chapter 4.....	31
Experimental Setup	31
4.1. LCVD System.....	31
4.2. Experimental Design of LCVD Graphene on Ni and Pt Foil	33
Chapter 5.....	36
Results and Discussions	36
5.1. LCVD Graphene on Ni Foil	36
5.1.1. Thickness optimization	36
5.1.2. Gas mixture and scanning rate variation under a high base pressure.....	41
5.1.3. Gas mixture and scanning rate variation under a low base pressure	43
5.1.4. Scanning rate optimization.....	46
5.2. LCVD Graphene on Pt Foil	50
Chapter 6.....	54
Conclusions and Outlook.....	54
6.1. Conclusions.....	54

6.2. Outlook	56
Acknowledgement	58
Bibliography	59

List of Figures

- Figure 1. 1. Graphene serves as a building block for other carbon materials in any dimensions. It can be wrapped into fullerene, rolled into a carbon nanotube, and stacked into graphite. Fig.1.1. is adapted from [1]. 10
- Figure 2. 1. a) The energy diagram of the electronic configuration of the ground state and excited state in a carbon atom. b) An illustration of the orbitals of sp^2 hybridization which form three σ bonds. c) Honeycomb lattice with sublattice A and B and d) its corresponding reciprocal lattice of graphene structure. Figure a) and b) are adapted from [39] while figure c) and d) are adapted from [38]. 15
- Figure 2. 2. a) The electronic structure of graphene based on a tight binding model with the nearest neighbor approximation. b) The linear dispersion of energy-momentum relation of graphene around the K point. c) The electronic structure of graphene based on a tight binding model with next nearest neighbor approximation. d) Cut through the electronic band structure from $K \rightarrow \Gamma \rightarrow M \rightarrow K$. There is symmetry breaking of the valence (π) and conduction (π^*) band when taking the next nearest neighbor hopping is taken into account. Figure a) is adapted from [38], figure b), figure c) and d) are adapted from [39]. 16
- Figure 2. 3. Four basic adsorption arrangements for non-rotated graphene on hexagonal metal surfaces. a) hollow site arrangement, b) atop site/fcc'-hollow site arrangement, c) atop site/hcp'-hollow site arrangement, d) bridge arrangement. This figure is adapted from [15]. 18
- Figure 2. 4. a) Schematic drawing of a domain boundary for graphene on a Ni(111) substrate b) STM image showing the structure of the domain boundary. c) The contrast around the boundary increases. The cross section taken along the white line indicates the exponential decay and is shown in the inset c). These figures are adapted from [46]. 19
- Figure 2. 5. a) ARPES measurements of graphene grown on Ni(111). The π band is downshifted by 2 eV as an indication of strong coupling between graphene and Ni(111). b) ARPES measurements after intercalation of a monolayer of Au. c) The linear band dispersion at the Dirac point is observed after intercalation of Au. It indicates that after intercalation graphene decouples from the Ni-substrate and forms quasi-freestanding graphene. These figures are adapted from [41]. 20
- Figure 2. 6. a) An illustration of the Moiré pattern of graphene on Pt(111) with $3 \times 3 G$ periodicity, and b) Moiré pattern with $44 \times 44 R_{15G}$. c) A close-up image of the ARPES map of the graphene π band near the K point of the Brillouin zone close to the Fermi energy in a direction perpendicular to $\Gamma - K$ in which both branches of the band are symmetric. These figures are adapted from [42]. 21
- Figure 3. 1. a) Energy level diagram of the Raman scattering processes leading to Stokes and anti-Stokes scattering. b) Experimental setup for measuring the Raman spectrum of a particular sample. c) Typical Raman spectrum of graphene. Fig. 2.1(a-b) are adapted from [53] and Fig. 2.1c is adapted from [52]. 23

Figure 3. 2. a) The interaction volume of a sample when interacting with a beam of primary electrons. b) Schematic SEM setup. SEM image of graphene grown on c) Ni foil and d) Pt foil. Fig. 2.2a is adapted from [56], Fig. 2.2b is adapted from [58]. Fig. 2.2(c-d) are adapted from [59] and [60], respectively...	25
Figure 3. 3. The graphene growth mechanism may be distinguished into a) a carbon segregation mechanism and d) a surface reaction mechanism. c) Experimental setup for CVD growth of graphene. Fig. 2.3(a-b) are adapted from [64].....	28
Figure 3. 4. a) Illustration of the LCVD process where the laser beam irradiates the substrate. A and B represent the molecules present in the chamber during the heating process of the laser beam [76]. b) Experimental setup of LCVD for direct laser writing of graphene. Fig. 2.4a is adapted from [76] and Fig. 2.4b is adapted from [79].....	29
Figure 4. 1. a) Scheme of the LCVD system. The laser beam path is aligned by using a mirror and lens attached to a motorized stage. By moving the motorized stage in x direction using a computer, we are able to scan the laser beam on the sample. b) The home-built chamber is attached to the translation stage. This chamber is equipped with an aluminum bracket to hold the gas sources which are connected to the pumping system. c) The translation stage is controlled by a micrometer screw and can be moved in three directions (x , y , and z -direction).....	32
Figure 4. 2. Illustration of how the Raman measurements were performed on the samples. The laser of the Raman setup was moved slowly across the sample to find the desired signal. The red arrow illustrates the direction of the Raman laser while the black lines indicate the 'invisible' laser pathway.	34
Figure 5. 1. a) Optical image (top) of Ni foil with 16 μm thickness exposed to the laser with a power of 2 Watts, optical image (middle) of Ni foil with 25 μm thickness exposed by the laser with a power of 4.5 Watts, and optical image (middle) of Ni foil with 125 μm thickness after exposed by the laser with a power of 4.5 Watts, b) A typical Raman spectrum that was measured around the laser pathway (region B) regardless the power, gas mixture, and scanning rate used in the experiments. c) A typical Raman spectrum that was measured either in the laser pathway (region C) or in the shadow (region D) of the 25 μm foil regardless the power, gas mixture, and scanning rate used in the experiment. c) A typical Raman spectrum of Ni foil with 125- μm thickness. The bar scale in the optical image is 100 μm	38
Figure 5. 2. The gas mixture variation used in the experiments under a base pressure of 10^{-3} mbar. 41	
Figure 5. 3. Optical image of Ni foil with 25 μm thickness exposed to the laser at a power of 4.5 Watts with a scanning rate of a) 10 $\mu\text{m/s}$, b) 20 $\mu\text{m/s}$, and c) 50 $\mu\text{m/s}$. All samples with variations of the gas mixture showed these typical images. d) A typical Raman spectrum measured inside the line regardless the gas mixture and the scanning rate used in the experiment. The scale bar in each optical image is 100 μm	42
Figure 5. 4. The gas mixture variations used in the experiments under a base pressure of 10^{-7} mbar.43	
Figure 5. 5. a) A typical image of the samples under a base pressure of 10^{-7} mbar. The scale bar is 100 μm . The three typical Raman spectra observed on each foil are b) the background spectrum, c) a typical	

spectrum for MLG (showing D band; 1340 cm^{-1} , G; 1583 cm^{-1} band and 2D-band region) and d) the spectrum related to ta-C: H.	44
Figure 5. 6. The four typical spectra observed are a) the background spectrum, b) MLG spectrum, c) ta-C: H spectrum, and d) a-C: H spectrum.....	47
Figure 5. 7. a) SEM image of MLG flakes grown on Ni foil by using a gas mixture of 6×10^{-3} mbar of CH_4 and 1×10^{-3} mbar of H_2 and the scanning rate of $50\text{ }\mu\text{m/s}$. The laser pathway is shown as the region A. It can be seen clearly the border between the line and its surrounding. b) The zoom-in image of the region A, c) region B, and d) region C which is the bare Ni foil. The scale bar in each figure is $100\text{ }\mu\text{m}$	49
Figure 5. 8. a) A typical optical image of Pt foil after LCVD experiment was completed. The scale bar is $100\text{ }\mu\text{m}$ The three typical spectra observed in the Raman measurement are b) the background spectrum, c) typical spectrum for MLG and d) the spectrum related to ta-C: H.	51
Figure 5. 9. a) SEM image of multilayer graphene flakes grown on Pt foil with a recipe of 6 to 1 ratio of methane and hydrogen and the scanning rate was $50\text{ }\mu\text{m/s}$. The laser path is shown as domains of graphene flakes. The scale bar is $100\text{ }\mu\text{m}$ b) The zoom-in image of the line. There were domains and a wrinkled sheet of graphene flakes. The scale bar is $100\text{ }\mu\text{m}$. c) SEM image of another laser pathway on Pt foil, indicated by the dashed line. The scale bar is $200\text{ }\mu\text{m}$ d) The zoom-in image of the line area shows one isolated flake of graphene. The scale bar is $10\text{ }\mu\text{m}$	52
Figure 6. 1. The SEM image of a) the laser pathway on Ni foil (the scale bar is $100\text{ }\mu\text{m}$), b) inside the laser pathway on Ni foil (the scale bar is $100\text{ }\mu\text{m}$), c) the laser pathway on Pt foil (the scale bar is $100\text{ }\mu\text{m}$), and d) isolated single domain graphene on Pt foil (the scale bar is $10\text{ }\mu\text{m}$).	55

List of Tables

Table 4. 1. Parameters used by Park et al. to grow a line of graphene using LCVD technique.....	33
Table 5. 1. The variations of parameters in the thickness optimization experiment.....	37
Table 5. 2. The number of MLG spectra and amorphous carbon spectra recorded from all samples.	45
Table 5. 3. The number of MLG, ta-C: H, and a-C: H spectra from all samples.	48

Chapter 1

Introduction

1.1. General Introduction

Graphene is a single layer of carbon atoms tightly packed into a two-dimensional honeycomb lattice. It is the building block for other dimensionalities of sp^2 hybridized carbon allotropes. This material can be wrapped into a zero-dimensional fullerene, rolled into a one-dimensional carbon nanotube, and stacked layer by layer into three-dimensional graphite (see fig. 2.1) [1]. The term of graphene for this single layer carbon material was first introduced by Boehm, Setton, and Stump in 1994 [2]. For several decades, the single layer of isolated graphene seemed to be theoretically impossible since it was considered to be thermodynamically not stable [3]. However, Geim and Novoselov reported a method, namely micromechanical cleavage or the so-called scotch tape method, for producing single layer graphene on a SiO_2 substrate by peeling a graphite [4]. This discovery was an important step delivered in 2004, and six years later Geim and Novoselov were honored with the Nobel Prize in Physics for groundbreaking experiments regarding the two-dimensional material graphene [5].

Wallace already showed in early 1947 that a single sheet of sp^2 hybridized carbon has a linear energy dispersion as a function of momentum space at the K-point of the first Brillouin zone [6]. It turns out that this linear dispersion behavior gives rise to unusual physical properties [7]. Graphene has a high intrinsic mobility ($2 \times 10^5 \text{ cm}^2 \text{Vs}^{-1}$) [8, 9, 10], high Young's modulus (1.0 TPa) [11], high thermal conductivity ($\sim 5000 \text{ Wm}^{-1} \text{K}^{-1}$) [12], good electrical conductivity (the resistivity of pristine graphene is around $10^{-6} \text{ }\Omega\text{cm}$) [13], and high transmittance ($\sim 97.7 \%$) [14]. Moreover, these outstanding properties make graphene a great potential material for many applications in electronic, transparent and flexible electrodes, sensors, energy conversion and storage devices [13] [14].

Those unique properties of graphene have motivated many studies on this excellent material. Up to now, graphene research may be divided into three sub-areas. The first is associated with the special physical properties generated by the 2D nature of graphene. The second one is the research on device applications of graphene while the last one is about the material science of graphene including producing and processing of graphene [15]. In this master thesis, the work primarily revolves around the last one.

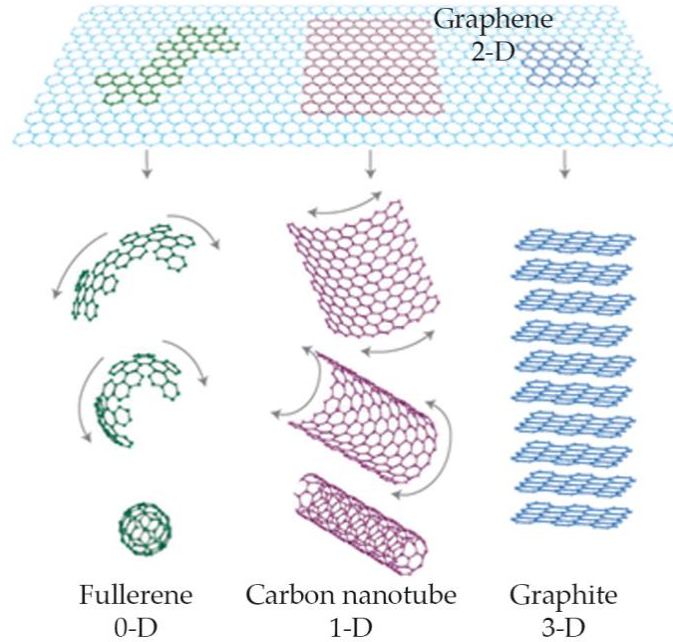


Figure 1. 1. Graphene serves as a building block for other carbon materials in any dimensions. It can be wrapped into fullerene, rolled into a carbon nanotube, and stacked into graphite. Fig.1.1. is adapted from [1].

In general, there are two approaches to produce graphene, top-down and bottom-up approaches. In the former, graphene is obtained by reducing bulk materials, e.g. graphite, into graphene flakes. However, the latter one consists of techniques that produce graphene from smaller building block materials [16] [17]. The review of both top-down and bottom-up approaches to fabricate graphene can be found in the article of Bhuyan et. al. [17]. Some of the examples of top-down fabrication of graphene are micromechanical exfoliation from graphite [4], direct sonication of graphite [18], and electrochemical exfoliation [19] while the examples of the bottom-up approaches are Chemical Vapor Deposition (CVD) [20], confined self-assembly [21], arc discharge [22], epitaxial growth on SiC [23], unzipping of carbon nanotubes [24], and reduction of CO [25].

One of the most studied methods to grow graphene is the CVD technique because in general, it can readily generate continuous large graphene sheets in high quality [15]. This technique employs hydrocarbons as the precursor gas and transition metals as the catalyst. Several transition metals such as Ni [26], Cu [27], Ir [28], Pd [29] and Ru [30], have been used as catalysts in graphene production. Although the research of graphene synthesis has developed, the integration of graphene into practical circuits for technology purposes remains challenging. This is because the integration needs a pattern of graphene on the particular substrate. A pattern of

graphene is commonly created through lithography processes that require multiple steps which can be very time-consuming [31].

Recently, direct laser writing (DLW) has emerged as a promising technique for rapidly patterning graphene, such as laser thinning of graphene [32], laser patterning of CVD graphene [33], laser patterning of graphene oxide [34], and laser assisted chemical vapor deposition (LCVD) [35] [36]. The first three methods combine procedures of graphene growth and laser patterning while the last method is truly a single step of patterning graphene. LCVD can be used for synthesis and patterning simultaneously. LCVD does not need a furnace like in conventional CVD since it relies on the interaction between a laser and the substrate to generate high temperature. Furthermore, the pattern of graphene can be directly fabricated without annealing, cooling, and post processing such as in lithography. LCVD also shortens the growth time from several hours to a few seconds so that a pattern of graphene can be synthesized fast [35, 36, 37].

Park et al. [35] and Jiang et al. [36] reported the possibility of patterning high-quality graphene by means of LCVD. Park et al. synthesized graphene on Ni foil with a focused continuous wave (CW) laser (optically pumped solid-state laser; 532 nm) as the heat source. The authors studied the possibility of patterning graphene on Ni foil without further study of the LCVD parameters dependence on the growth mechanism [35]. Jian et. al. demonstrated how to synthesize graphene via LCVD technique with a 600 W continuous wave fiber laser focused on 1 mm with a wavelength of 1060 nm. The authors studied how the scanning rate and the laser power affected the few-layer-graphene growth on Ni by means of LCVD [36]. Herein, we would like to study how parameters important for the LCVD process affect the graphene growth on Ni foil. We conducted a systematic study to optimize LCVD parameters like the thickness of the Ni foil, the gas mixture, the base pressure of the chamber, the laser power, the beam diameter, and the scanning rate. The result of this optimization study, which is the recipe for growing graphene on Ni foil by using LCVD, was also applied to Pt foil as the substrate.

1.2. Research Goal

In this work, it was the goal to obtain a recipe for growing graphene on Ni foil by using the LCVD technique and to apply the obtained recipe to Pt foil. We conducted three steps to achieve these goals. In the first step, we designed, implemented, and tested a simple home-made LCVD setup suitable for graphene growth. The second step was the systematic study to obtain a recipe for graphene growth on Ni foils. In this step, we studied how the thickness of the Ni foil, the gas mixture, the base pressure of the chamber, the laser power, the beam diameter, and the scanning rate influenced the graphene growth on Ni foil. The third step was implementing the recipe obtained from the previous systematic study to Pt foils.

1.3. Thesis Structure Overview

This thesis contains the following chapters; Chapter 1 gives an introduction. Chapter 2 gives a general overview of the characteristics of graphene. Chapter 3 summarizes the techniques and characterization methods used in this work. The experimental setup and its implementation regarding the LCVD technique are described in Chapter 4, while the results and discussions are reported in Chapter 5. The conclusions of the thesis and the outlook are described in Chapter 6.

Chapter 2

Graphene

In this chapter, we only highlight the properties of graphene which are relevant to our work. Those topics include the structure of graphene, its electronic band structure, and the interfaces between graphene and transition metals, namely nickel and platinum. The first two parts are meant to introduce the reader to both structure and electronic band structure of graphene. The last part is relevant for the growth of graphene on Ni and Pt foils.

2.1. The sp^2 Hybridization in Graphene

The following explanation about the structure and electronic band structure is mostly based on the book of Katsnelson [38] and the lecture notes of Fuchs and Goerbig [39]. For a more comprehensive review of electronic properties of graphene, the reader may refer to ref. [40].

Graphene consists of carbon atoms as its building blocks. The carbon atom has six electrons with the configuration $1s^2 2s^2 2p^2$ in the ground state. It is energetically favorable to completely fill the electrons in the 1s and 2s state and put the other two in the 2p states (illustrated in Fig. 2.1.a) because the 2p states ($|2p_x\rangle$, $|2p_y\rangle$, and $|2p_z\rangle$) are roughly 4 eV higher than the 2s state. However, when the carbon atoms form molecules or solids, the gained energy to form the covalent bond is larger than 4 eV. Thus, it is favorable to excite one electron from the 2s to the third 2p orbital (illustrated in fig. 2.1.a) [38, 39].

According to quantum mechanical theory, this excited state constructs four equivalent quantum-mechanical states, $|2s\rangle$, $|2p_x\rangle$, $|2p_y\rangle$, and $|2p_z\rangle$. A superposition of the state $|2s\rangle$ with $n|2p_j\rangle$ states is called sp^n hybridization, which plays an essential role in covalent carbon bonds and influences the arrangement of carbon atoms when linked to other atoms [39].

Graphene is arranged by sp^2 hybridized carbon atoms. The $|2s\rangle$ state mixes with two of $|2p_j\rangle$ states, which may be chosen to be $|2p_x\rangle$ and $|2p_y\rangle$ states. The representation of quantum-mechanical states for this hybridization may be written as [39]

$$\begin{aligned}
|sp_1^2\rangle &= \frac{1}{\sqrt{3}}|2s\rangle - \sqrt{\frac{2}{3}}|2p_y\rangle, \\
|sp_2^2\rangle &= \frac{1}{\sqrt{3}}|2s\rangle + \sqrt{\frac{2}{3}}\left(\frac{\sqrt{3}}{2}|2p_x\rangle + \frac{1}{2}|2p_y\rangle\right), \\
|sp_3^2\rangle &= -\frac{1}{\sqrt{3}}|2s\rangle + \sqrt{\frac{2}{3}}\left(-\frac{\sqrt{3}}{2}|2p_x\rangle + \frac{1}{2}|2p_y\rangle\right).
\end{aligned} \tag{1}$$

The corresponding orbitals are oriented in the x-y plane and form three σ bonds (see Fig. 2.1.b). The remaining unhybridized $|2p_z\rangle$ orbital is perpendicular to the plane and forms a π bond [39]. Due to these properties of the sp^2 hybridization, the carbon atoms in graphene arrange in a honeycomb lattice [39]. This lattice can be seen as a combination of two triangular Bravais lattices, sub-lattice A and B (Fig. 2.1.c), with the lattice vectors as

$$\vec{a}_1 = \frac{a}{2}(3, \sqrt{3}), \quad \vec{a}_2 = \frac{a}{2}(3, -\sqrt{3}), \tag{2}$$

where $a \approx 1.42\text{\AA}$ is the nearest-neighbor distance corresponding to a conjugated carbon-carbon bond [38].

Each atom from sublattice A is surrounded by three atoms from sublattice B and vice versa. These surrounding atoms are the nearest neighbor atoms and are connected to sublattice A with lattice vectors [38]

$$\delta_1 = \frac{a}{2}(1, \sqrt{3}), \quad \delta_2 = \frac{a}{2}(1, -\sqrt{3}), \quad \delta_3 = a(-1, 0). \tag{3}$$

The reciprocal lattice of graphene is a triangular lattice (Fig. 2.1.d) with the lattice vectors [38]

$$b_1 = \frac{2\pi}{3a}(1, \sqrt{3}), \quad b_2 = \frac{2\pi}{3a}(1, -\sqrt{3}). \tag{4}$$

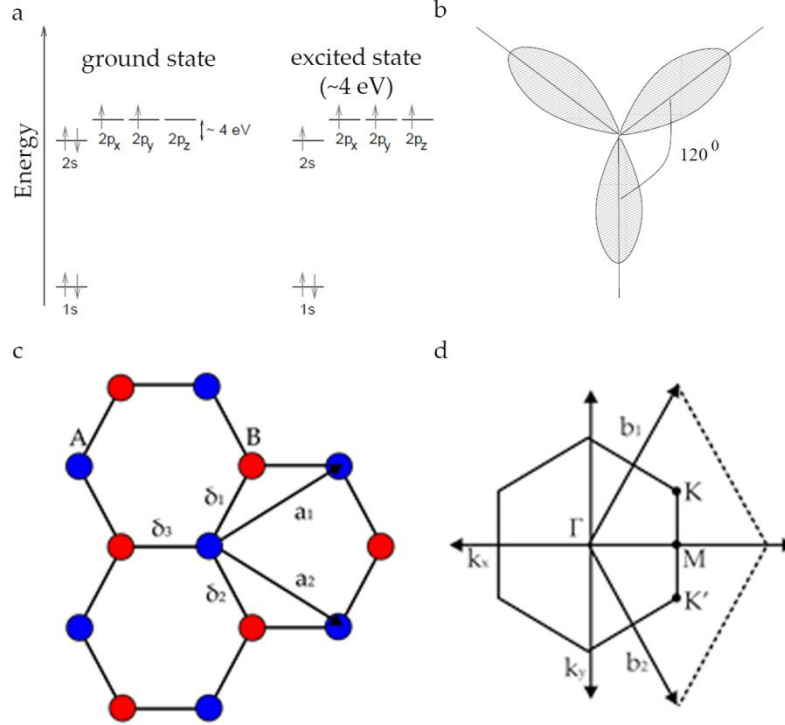


Figure 2. 1. a) The energy diagram of the electronic configuration of the ground state and excited state in a carbon atom. b) An illustration of the orbitals of sp^2 hybridization which form three σ bonds. c) Honeycomb lattice with sublattice A and B and d) its corresponding reciprocal lattice of graphene structure. Fig. a) and b) are adapted from [39] while fig. c) and d) are adapted from [38].

2.2. Electronic Band Structure of Graphene

In the graphene structure, the π electrons are responsible for the electronic properties at lower energies, whereas the σ electrons form energy bands far away from the Fermi energy. Thus, the discussion of energy bands of π electron is relevant to obtain the insight to the origin of the peculiar electronic properties of graphene [38, 39]. The electronic band structure of graphene was originally calculated by Wallace, already in 1947 [6].

In the honeycomb lattice, the wavefunction basis contains two states belonging to two π electrons in the atoms from sublattices A and B. For the nearest-neighbor approximation, the tight-binding Hamiltonian is then described by a 2×2 matrix as [38]

$$\hat{H}(\vec{k}) = \begin{pmatrix} 0 & tS(\vec{k}) \\ tS^*(\vec{k}) & 0 \end{pmatrix} \quad (5)$$

where t is the hopping parameter of the nearest neighbor, \vec{k} is the wave vector, and $S(\vec{k})$ is the orbital overlap matrix

$$S(\vec{k}) = \sum_{\vec{\delta}} e^{i\vec{k}\vec{\delta}} = 2 \exp\left(\frac{ik_x a}{2}\right) \cos\left(\frac{k_y a \sqrt{3}}{2}\right) + \exp(ik_x a) \quad (6)$$

where $\vec{\delta}$ is the lattice vector of the nearest neighbor.

In the following, the hopping from the next-nearest neighbor is neglected. By solving the eigenvalue of Schrodinger equation with abovementioned Hamiltonian, one obtains the energy dispersion relation as

$$E(\vec{k}) = \pm t |S(\vec{k})| = \pm t \sqrt{3 + f(\vec{k})} \quad (7)$$

where

$$f(\vec{k}) = 2 \cos(\sqrt{3}k_y a) + 4 \cos\left(\frac{\sqrt{3}}{2}k_y a\right) \cos\left(\frac{3}{2}k_x a\right) \quad (8)$$

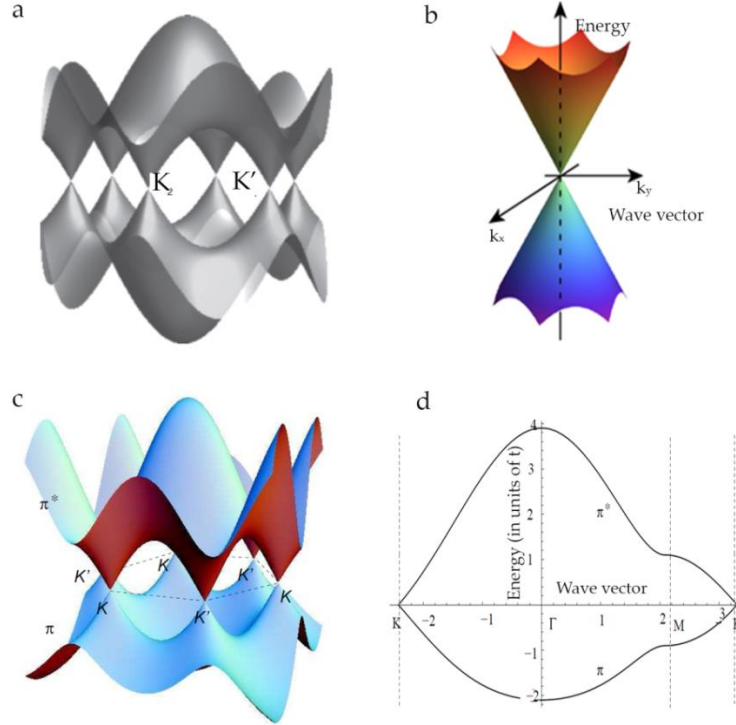


Figure 2. 2. a) The electronic structure of graphene based on a tight binding model with the nearest neighbor approximation. b) The linear dispersion of energy-momentum relation of graphene around the K point. c) The electronic structure of graphene based on a tight binding model with next nearest neighbor approximation. d) Cut through the electronic band structure from $K \rightarrow \Gamma \rightarrow M \rightarrow K$. There is symmetry breaking of the valence (π) and conduction (π^*) band when taking the next nearest neighbor hopping is taken into account. Figure a) is adapted from [38], figure b), figure c) and d) are adapted from [39].

This energy dispersion relation is illustrated in the Fig. 2.2a. which shows that the occupied and unoccupied site are fully symmetric due to the absence of the next nearest neighbor hopping [38]. One can immediately see that $S(\vec{K}) = S(\vec{K}') = 0$, which means band crossing in the K and K' point [38].

where

$$\vec{K} = \left(\frac{2\pi}{3a}, -\frac{2\pi}{3\sqrt{3}}\right), \quad \vec{K}' = \left(\frac{2\pi}{3a}, \frac{2\pi}{3\sqrt{3}}\right). \quad (9)$$

By expanding the Hamiltonian near the K or K' point, one can find the effective Hamiltonian near those points. The eigenvalue for Schrodinger equation with the effective Hamiltonian results the linear dispersion of energy spectrum around K or K' point (illustrated in fig. 2.2. b) [38].

By taking into account the next-nearest neighbor hopping t' , eq. (7) is modified into

$$E(\vec{k}) = \pm t|S(\vec{k})| + t'f(\vec{k}) = \pm t\sqrt{3 + f(\vec{k})} + t'f(\vec{k}) \quad (10)$$

It is clear that the second term in Eq. (10) breaks the symmetry between the occupied and unoccupied site. A 2-D plot and 1-D plot along characteristic points in the first Brillouin zone are shown in Fig. 2.2.c and Fig. 2.2.d, respectively. However, this symmetry breaking does not change the linear behavior of the energy dispersion around the K point, which is a characteristic of the peculiar electronic structure of graphene and the origin of its unique electronic properties [38] [39].

2.3. Graphene-Metal Interfaces

The interaction between graphene and transition metals can be distinguished between strong and weak interaction. Batzill et al. summarized in the review paper regarding these interactions [15]. Strong interaction means that the coupling of graphene and metal is strong enough to open a band gap. Thus, the properties of graphene are no longer the same as those of pristine graphene. On the other hand, weak interaction means that the coupling between graphene and the metal is low, hence protecting the properties of pristine graphene (quasi-free-standing graphene) [15]. Nickel is one of the strong-interacting elements [41] while platinum is weakly coupled to graphene [42].

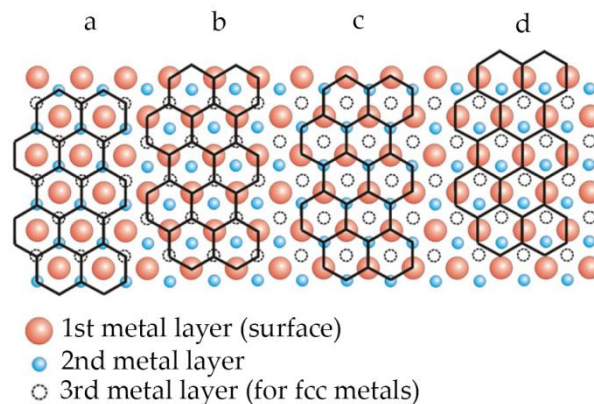


Figure 2. 3. Four basic adsorption arrangements for non-rotated graphene on hexagonal metal surfaces. a) hollow site arrangement), b) atop site/fcc'-hollow site arrangement, c) atop site/hcp'-hollow site arrangement, d) bridge arrangement. This figure is adapted from [15].

The carbon atoms of graphene can be seen as adsorbates on the metal surface. There are four basic adsorption arrangements for non-rotated graphene on hexagonal (fcc (111) or hcp (0001)) metal surface (illustrated in Fig. 2.3). The first arrangement is that the carbon atoms of graphene are located in three-fold hollow sites (fig. 2.3a). The second one is that carbon atoms alternately occupy on metal atop and fcc-hollow site (fig. 2.3b). The third one is that carbon atoms alternately occupy on metal atop and hcp-hollow site (fig. 2.3c). The fourth arrangement is known as bridge-arrangement (fig. 2.3d) [15].

Graphene on Ni(111)

The study of graphene-nickel interfaces dates back to the early study of single and multilayer graphene formation on carbon saturated Ni(111) by Shelton et.al [43]. The authors studied the temperature dependence of graphene on carbon saturated Ni(111) using Auger electron spectroscopy (AES). A further study of a single layer graphene on Ni(111) was conducted by Gamo et al. [44]. They showed the growth of a commensurate graphene overlayer on Ni(111).

Ni(111) is a unique substrate for graphene growth since it has a good lattice match with graphene. This close lattice match allows for large domains without the formation of a Moiré pattern¹ [15] [44]. Graphene can grow on the Ni substrate with two different adsorption configurations, the fcc-hollow one (fig.2.3b) and hcp-hollow one (fig. 2.3c). This is because the adsorption energies for these two configurations are very similar [45]. These two configurations may be present on the sample and result in a domain. The resulting domain boundaries were studied using STM by Lahiri et.al [46]. The boundary between these domains is illustrated in fig.

¹ A Moiré pattern is a superstructure of misalignment between two periodic lattices. This pattern can be observed when graphene layer is rotated with respect to the surface of the substrate

2.4a. At the boundary, the STM study showed that the carbon atoms restructure into pairs of pentagons and octagons (see fig. 2.4b) [46]. Moreover, the boundary can only form along one crystallographic direction of the graphene. This boundary has a metal characteristic whose metallic state decays exponentially into the neighboring graphene lattice. This state can be seen as an increased contrast in STM around the boundary (fig. 2.4c) [46].

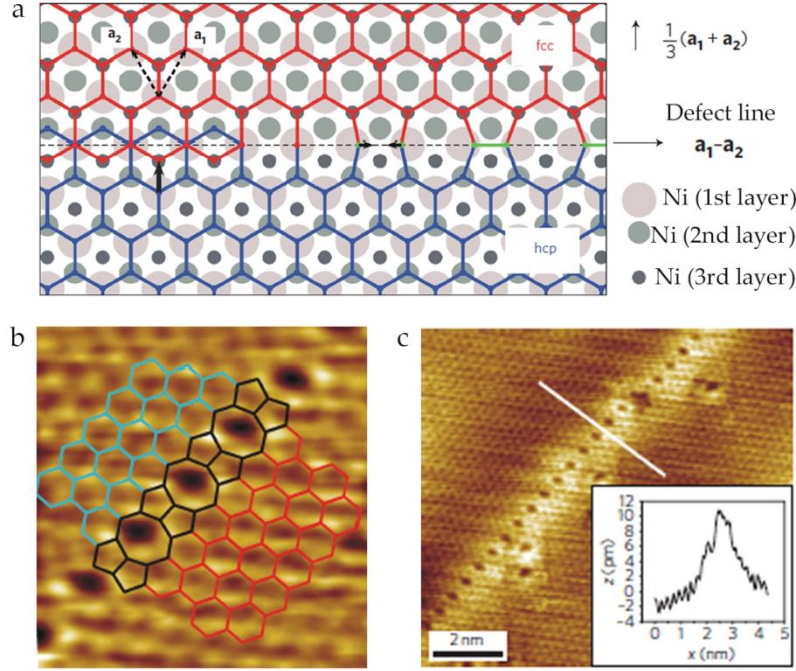


Figure 2. 4. a) Schematic drawing of a domain boundary for graphene on a Ni(111) substrate b) STM image showing the structure of the domain boundary. c) The contrast around the boundary increases. The cross section taken along the white line indicates the exponential decay and is shown in the inset c). These figures are adapted from [46].

The coupling between graphene and Ni(111) surface is strong enough to induce a band gap at the K-point. Evidence for this interaction is that the vertical separation between graphene and Ni(111) is 2.11 Å and 2.16 Å from graphene's carbon atoms at the fcc-hollow and atop carbon sites, respectively [44]. Moreover, several ARPES studies of the electronic structure of graphene on Ni(111) showed a downward shift of the π states by about 2 eV [41, 47, 48] and the opening of a band gap at the K-point. Fig. 2.5 shows the comparison of ARPES data of graphene on Ni(111) (fig. 2.5.a) and formation of quasi-free-standing graphene after Au-intercalation (2.5.b). In the close-up ARPES map around the K point (Fig. 2.5.c), the linear dispersion of graphene's band structure is observed at the Dirac point.

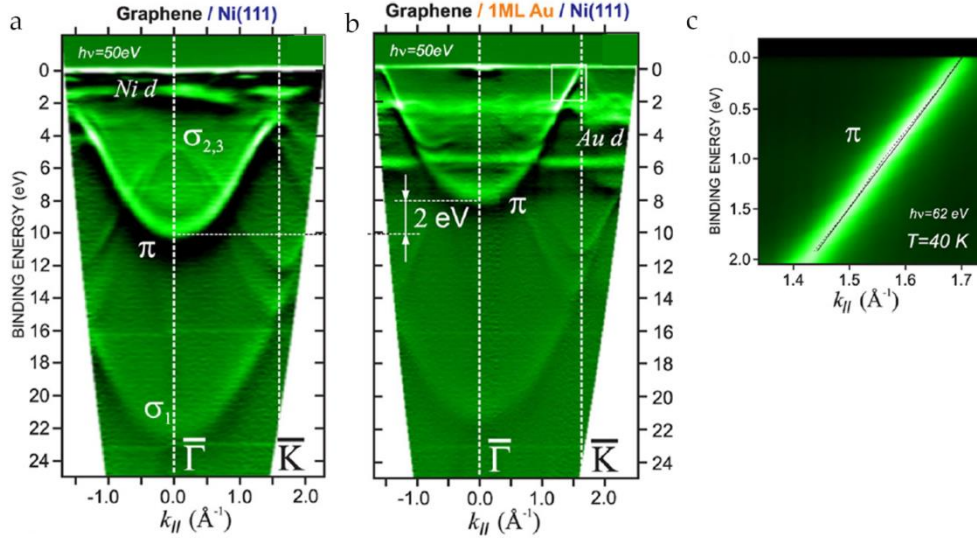


Figure 2. 5. a) ARPES measurements of graphene grown on Ni(111). The π band is downshifted by 2 eV as an indication of strong coupling between graphene and Ni(111). b) ARPES measurements after intercalation of a monolayer of Au. c) The linear band dispersion at the Dirac point is observed after intercalation of Au. It indicates that after intercalation graphene decouples from the Ni-substrate and forms quasi-freestanding graphene. These figures are adapted from [41].

Graphene on Pt(111)

Graphene on platinum behaves differently from graphene on nickel. The interaction between single layer graphene and Pt(111) is considered weak as the pristine properties of single layer graphene are preserved. This weak interaction is a consequence of graphene arrangement on platinum, the separation between graphene and platinum surface, and the band structure of graphene coupled to platinum [42].

The structure of graphene on Pt(111) has been studied by Sutter et.al in 2009 [42]. The authors observed that graphene has a mismatched lattice with Pt(111) leading to the formation of Moiré patterns with specific angles. They found various Moiré patterns having different unit cells. Figure 2.6.a and 2.6.b illustrate a small unit cell with $(3 \times 3)_C$ periodicity and a large unit cell with $(\sqrt{44} \times \sqrt{44})R15_C$ periodicity, respectively. It turns out that none of these structures is dominant. This means that there are only small energy differences among the Moiré patterns [42]. However, Merino et al. suggested that the structure with a small mismatch lattice is considered more favorable [49].

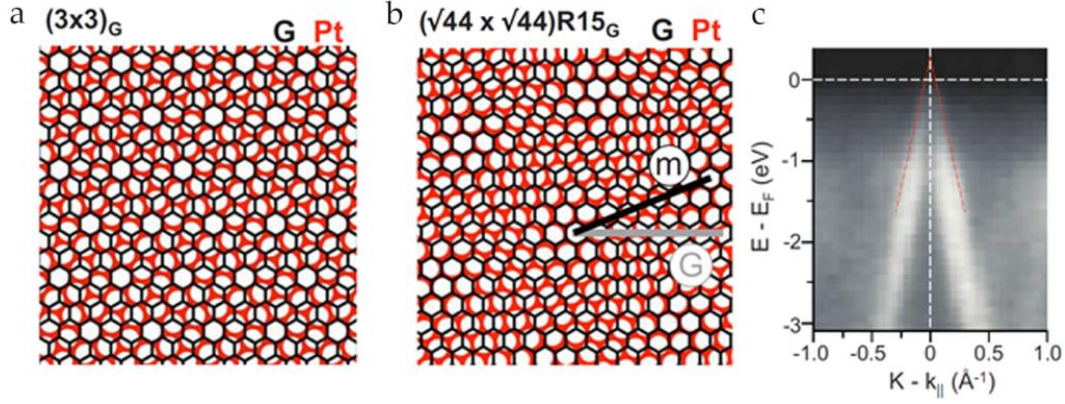


Figure 2. 6. a) An illustration of the Moiré pattern of graphene on Pt(111) with $(3 \times 3)_G$ periodicity, and b) Moiré pattern with $(\sqrt{44} \times \sqrt{44})R15_G$. c) A close-up image of the ARPES map of the graphene π band near the K point of the Brillouin zone close to the Fermi energy in a direction perpendicular to $\Gamma - K$ in which both branches of the band are symmetric. These figures are adapted from [42].

Theoretical and experimental studies agree that the rotational structure of graphene on Pt(111) causes a separation between graphene and Pt(111) of 3.3 \AA which is similar to the spacing of graphene sheets in graphite of 3.36 \AA [42, 50]. This also suggests that the coupling between graphene and Pt(111) is weak [42]. Direct evidence for a weak coupling between monolayer graphene and Pt(111) is provided by a micro-ARPES study of its band structure (see Fig. 2.6.c). The electronic structure of monolayer graphene on Pt(111) is close to that of pristine graphene which exhibits linear π band at the K point [42].

Chapter 3

Characterization and Experimental Techniques

This chapter briefly presents the characterization methods as well as the experimental techniques utilized during this master project. Although it is far from comprehensive, this chapter will help the reader follow the results and discussions section. More insight into the techniques can be found in the cited references.

3.1. Raman Spectroscopy

Raman spectroscopy is a characterization technique based on the inelastic scattering of light by matter. It is nondestructive and noninvasive because it uses photons, which are massless and chargeless particles, as a probe to analyze the sample. Raman spectroscopy is one of the essential tools in nanoscience and nanotechnology because it is highly sensitive to the physical and chemical properties of materials as well as environmental effects changing these properties [51].

In Raman spectroscopy, an incident photon with certain energy reaches the sample and is scattered either elastically (Rayleigh scattering) or inelastically (Raman scattering). The process is depicted in the energy level diagram shown in figure 3.1a. Raman spectroscopy only takes into account the inelastic scattering in which the incident photon can decrease or increase its energy by creating (Stokes process) or destroying (anti-Stokes) a phonon excitation in the sample. Since the anti-Stokes signal is usually weaker than the Stokes process, it is common to focus on the Stokes spectra [51, 52].

The general Raman spectroscopy setup consists of a laser source (visible to near infrared) whose beam passes through a lens and then through a small mirror with a curved reflecting surface (see Fig. 3.1b). The focused beam strikes the sample, and the scattered light is both reflected and focused by the mirror into an analyzer. The spectrum is analyzed by a monochromator or interferometer and is then captured by the detector [53].

A typical Raman spectrum is a plot of the scattered intensity as a function of the energy difference between the laser energy and the scattered energy called Raman shift (commonly displayed in units of cm^{-1}) [51]. In this work, we used Raman spectroscopy to characterize the presence and quality of graphene grown by LCVD. As an integral part of graphene research, Raman spectroscopy cannot only prove the signature of graphene but also determine the number and orientation of graphene layers, quality, and types of graphene edges, as well as functional groups attached to graphene [52].

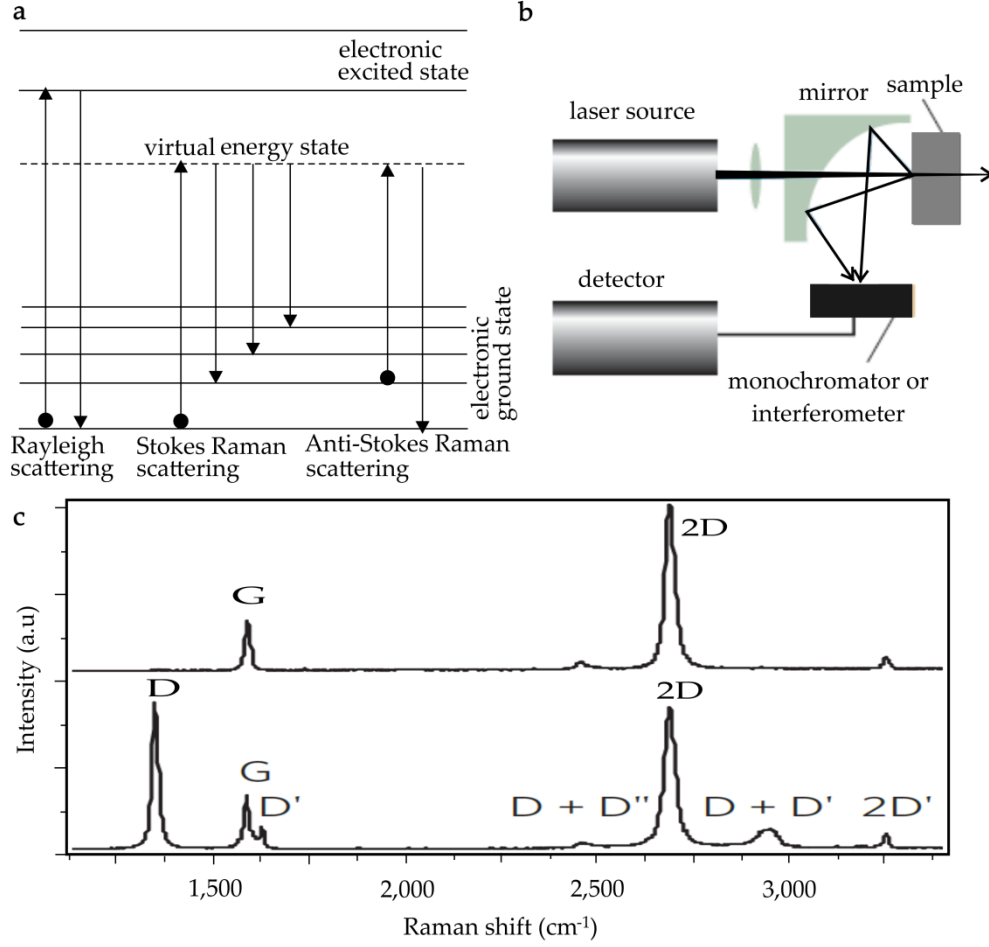


Figure 3. 1. a) Energy level diagram of the Raman scattering processes leading to Stokes and anti-Stokes scattering. b) Experimental setup for measuring the Raman spectrum of a particular sample. c) Typical Raman spectrum of graphene. Fig. 2.1(a-b) are adapted from [53] and Fig. 2.1c is adapted from [52].

The Raman spectrum of graphene (see Fig. 3.1c) exhibits a relatively simple structure that is usually characterized by two main bands designated as the G and 2D bands. When defects in graphene are present, a third D band appears. These bands differ in the positions, band shape, and relative intensity [52].

The G band is a characteristic peak appearing at 1587 cm⁻¹ in Raman spectra of graphene. Even though the band position is independent of the laser's energy, it is highly sensitive to the number of layers of graphene. As the number of layers increases, the G band position shifts to lower Raman shift. Moreover, this band position can also be affected by the temperature, doping in graphene, and even small amounts of strain present in the structure [52, 54].

The second band that is a signature of the presence of graphene is the 2D band. It usually appears as a high-intensity band in the spectrum and can also be used to determine the layer

thickness of graphene. In contrast to the G band, the number of layers influences not only the position of the 2D band but also its shape. The differences between single and multilayer graphene can be observed clearly in the symmetry of the 2D peak. For single layer graphene, this peak has a single symmetric shape, while for multilayer graphene it is asymmetric [52, 54]. The 2D band exhibits strong dispersive behavior, so the position and shape of the band can be significantly different when different laser excitation energies are used. Single layer graphene can be identified by analyzing the peak intensity ratio of the 2D and G bands which is equal to two for high quality (defect free) single layer graphene [52, 54].

The D band occurs if there are defects in the sample. It represents a ring breathing mode from a sp^2 carbon ring, which can be Raman active if the carbon ring is adjacent to the edge of graphene or a defect. This band is typically weak in graphene unless a lot of defects occur in the sample. Both its position and shape can significantly vary with the energy of the laser used [54]. The defects can be further characterized by the presence of other bands, such as the D' or D'' peak. For a detailed description of additional bands in Raman spectra of graphene, please refer to [52, 54].

The Raman spectra in this work were recorded using a Micro-Raman system RM 1000 RENISHAW, with excitation energy at 632.8 nm (Nd-YAG). The laser probe used had a spot size of around 10 micrometers.

3.2. Scanning Electron Microscopy

Scanning electron microscopy (SEM) is a surface-sensitive imaging technique that can provide topographical images of a sample surface with nanometer resolution. The image is obtained by rastering the sample surface with a high-energy beam of electrons [55]. This technique is based on the interaction of an incoming beam of electrons and the sample [56]. The detailed explanation of the SEM principle can be found in ref [55, 56, 57].

When a high-energy beam of electrons hits a sample, various radiation particles are produced and emitted from the sample. Each type of particle has its specific regions from which it emerges due to the interaction between the incoming primary electrons and the sample. Auger electrons are emitted from the topmost layers of the sample surface. Secondary electrons (SE) are expelled from the region around 5 nm from the surface. Backscattered electrons (BSE) emerge from deeper regions after the primary electrons experienced several scattering processes while penetrating the sample. Other products, such as continuous and characteristic X-rays are produced in an area around 10 μm from the sample surface [56]. This phenomenon is called the interaction volume and is shaped like a pear (illustrated in Fig. 3.2a).

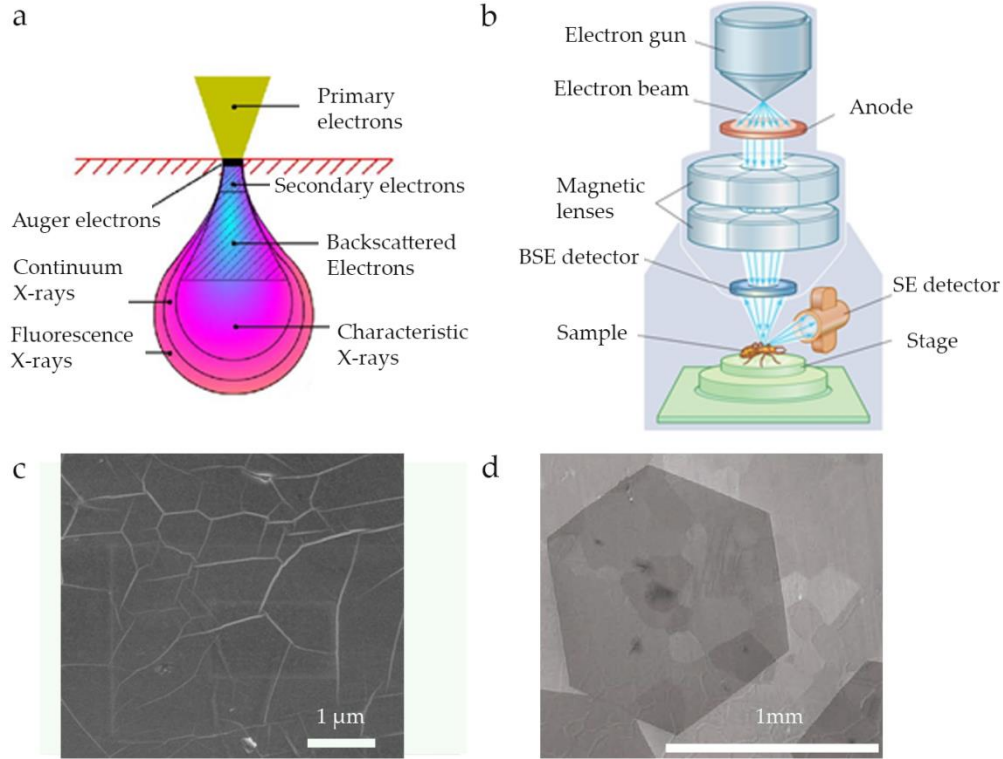


Figure 3. 2. a) The interaction volume of a sample when interacting with a beam of primary electrons. b) Schematic SEM setup. SEM image of graphene grown on c) Ni foil and d) Pt foil. Fig. 2.2a is adapted from [56], Fig. 2.2b is adapted from [58]. Fig. 2.2(c-d) are adapted from [59] and [60] , respectively.

In SEM, the topographical image of the sample surface is typically generated by detecting the SE (and BSE) [55, 56]. SE provide a detailed surface morphology of the sample while BSE image sharp contrast for two elements with different atomic numbers. The elements with high atomic numbers backscatter electrons more strongly than those with low atomic numbers. Both SE and BSE imaging can be combined to provide valuable information on both surface morphology of and elemental distribution within the samples [56].

A SEM setup consists of an electron gun, magnetic lens system, scanning system, and viewing system. Fig. 3.2b shows a schematic of a SEM configuration. A beam of electrons generated by the electron gun is accelerated towards the anode. It is condensed and focused by a series of magnetic lenses. The beam passes through the controllable coil magnets guiding the electron beam to scan across the sample surface in a raster-like pattern. The signal from SE (and BSE) is collected, amplified, and used to image the sample. The morphology of the sample surface is shown as distinct contrast on the screen [55, 61]. The spatial resolution of SEM images depends on the spot size of the beam scanned across the sample. Thus, the incident electron beam needs to be as small as possible to achieve high resolution. After focusing, the diameter of the

incoming beam is around 10 nm for a thermionic electron gun and around 1 nm for a field emission electron gun [56].

SEM images together with Raman spectra can provide a powerful tool to prove the presence of graphene flakes on a particular substrate. The Raman spectrum exhibits signatures of graphene, G, and 2D peak, while the SEM image provides a high-resolution image of graphene flakes. Figure 2.2c and 2.2d show a typical image for graphene grown on Ni foil [59] and Pt foil [60], respectively. It can be seen that the graphene flakes generate different contrast than the substrate. Graphene on Ni foil is indicated by wrinkles due to thermal stress during growth. This thermal stress is generally attributed to the difference between the thermal expansion coefficients of graphene and nickel [62]. Fig. 3.2c shows a graphene flake covering throughout the whole Ni substrate while Fig 3.2d shows a typical single domain graphene flake on Pt foil [60].

The SEM images in this work were recorded using a JEOL JSM 7000F field emission SEM with an electron energy of 5 keV.

3.3. Chemical Vapor Deposition

CVD is a technique for depositing a solid material on the desired substrate. The substrate is exposed by one or more precursors, which react on the substrate surface to produce the desired deposit. The deposited species could be atoms, molecules or a combination of these. A detailed discussion about the CVD process and theory can be found in the book of Pierson [63]. Recently, CVD is one of the most used methods to grow graphene on transition metals from a hydrocarbon precursor because it is inexpensive and produces large-area graphene. In CVD, the transition metal acts as catalysts for decomposing the hydrocarbon gas into carbon radicals that can then form single layer and multilayer graphene [64]. The CVD growth mechanism of graphene on transition metals may be divided into 2 general mechanisms, which are carbon segregation, and a surface reaction mechanism [64]. Pioneering works on graphene CVD were reported in 2008 and in 2009 [65, 66, 67].

Regarding its carbon solubility, the transition metal determines the mechanism of graphene growth. For a metal with high carbon solubility at elevated temperatures, such as nickel, the graphene growth is initiated by hydrocarbon decomposition into carbon that dissolves into the bulk (during heating) and the carbon then segregates to the surface (during cooling) to form graphene (see illustration in Fig. 3.3a) [64]. The fundamental limitation of utilizing high-carbon-soluble metals as the catalyst is that single and few-layer graphene is obtained over regions of a few tens of microns and not homogeneously over the entire substrate. The lack of control over the number of layers is partially attributed to the fact that the segregation of carbon from the

metal carbide upon cooling occurs rapidly within the metal grains and heterogeneously at the grain boundaries [68]. Metal with low carbon solubility at high temperature, such as copper, the growth mechanism of graphene is through surface reactions, which is in principle straightforward (see illustration in Fig. 3.3b). Graphene on such metals involves the decomposition of hydrocarbon gas into carbon radicals over a substrate typically held at 1000 °C, followed by carbon diffusion on the surface to form graphene [68]. This process can yield single layer graphene due to passivation of the surface. This process is independent of growth time or heating and cooling rates [67, 68].

The graphene growth mechanism on nickel is believed to be a segregation process [64, 69]. Graphene growth on nickel depends on the temperature [70], cooling rate [65] and hydrogen amount inside the CVD chamber [69]. Dahal et.al reviewed the temperature dependence of graphene growth on nickel. An ordered surface carbide is dominantly formed at the temperatures below 500 °C, which can be transformed into graphene if enough carbon is supplied. Temperature as 500-650 °C can ignite graphene growth on pure nickel. Graphene may be grown at the temperature as high as 650-900 °C when the carbon concentration in the bulk is saturated. However, at higher growth temperatures a significant fraction of the graphene domains is rotated with respect to the Ni(111) lattice. Upon cooling process, carbons segregate from the bulk underneath these rotated graphene domains and result either in carbide or second layer graphene formation [70]. The cooling rate in CVD process needs to be optimized in order to grow high-quality graphene. This cooling rate will affect the segregation behavior that strongly influences the thickness and quality of graphene [65]. The role of hydrogen in the CVD growth of graphene on nickel was studied by Losurdo et.al. It is suggested that optimizing the amount of hydrogen is important to produce high-quality graphene [69].

Platinum is a transition metal on which graphene growth occurs via carbon segregation processes. Weatherup et al. studied the growth mechanism of CVD graphene on Pt foil [71]. At high temperatures around 1000 °C, the hydrocarbons decompose into carbons that dissolve into the bulk Pt. Carbon supersaturations will develop locally close to the surface of Pt foil prior to graphene nucleation. Grain boundaries of Pt foil serve as rapid pathways for the carbon segregation, leading a nucleation of graphene domains. At the same time, this supersaturation is depleted. The graphene domains at grain boundaries approach one another to form a large domain. These processes occur at high temperature while the precursor is still supplied [71]. However, during cooling, Sun et al. suggested that carbon from the bulk still segregate into the surface to make second layer graphene [72].

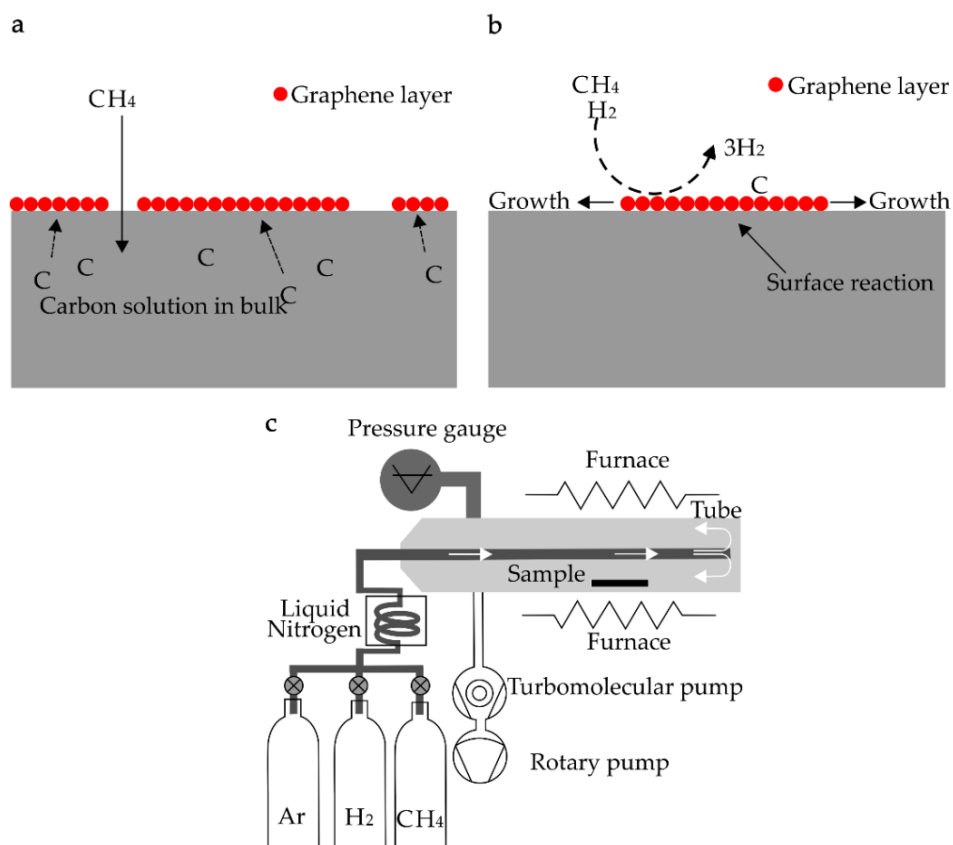


Figure 3. 3. The graphene growth mechanism may be distinguished into a) a carbon segregation mechanism and d) a surface reaction mechanism. c) Experimental setup for CVD growth of graphene. Fig. 2.3(a-b) are adapted from [64].

Fig. 3.3c depicts a typical CVD chamber utilized to grow graphene. The precursor gas used for growing graphene is a hydrocarbon gas, such as methane. The Ar gas is usually used to keep the partial pressure of the precursor gas constant [67, 69]. The presence of hydrogen gas is used to maintain the quality of the obtained graphene [69]. Liquid nitrogen is used to condense all impurities from gases [73]. The low pressure is achieved by pumping out the chamber with a turbo-molecular pump backed by a rotary pump. The heat is obtained from a furnace applied around the tube. The growth of graphene by CVD can be achieved by inserting the sample into the vacuum tube and heating the sample while flowing the precursor gas. CVD parameters, such as gas flow, total pressure, or temperature of the sample and cooling time, are optimized in order to obtain high quality and large area graphene [67, 74].

3.3. Laser-assisted Chemical Vapor Deposition

LCVD, a variant of CVD technique, is a technique for depositing a solid material on the laser-irradiated area of the substrate from one or more precursor gases. In general, there are two types of LCVD, photolytic and pyrolytic LCVD. Photolytic LCVD uses photons from a laser beam to

decompose the precursor gas. The decomposed molecules deposit on the surface along the laser path. In this technique, the wavelength of the laser and the precursor gas should be ‘tuned’ to react with each other. Pyrolytic LCVD uses a laser beam as a heat source to heat the surface of a substrate up to the temperature required for decomposing the precursor gas. The reactions are restricted to the heated zone under the laser spot. This zone is defined by the parameters of the laser, such as the laser power and beam diameter, and the thermal and optical properties of the substrate. In this work, we employ pyrolytic LCVD to grow graphene on Ni foils and Pt foils. We will name this technique as LCVD throughout the thesis [75, 76].

The LCVD process is schematically depicted in Fig. 3.4a. The laser light is absorbed by the substrate. For example, we have molecule AB that is decomposed under high temperature. We assume that atom A is relevant for surface reaction while atom B weakly interacts with the surface. If we ignore any heat flow into the ambient medium, molecule AB is decomposed only within the laser-heated area. While species A sticks to the surface or subsequently reacts with the substrate, species B desorb. This process is similar to that in conventional CVD [76]. LCVD differs from conventional CVD in that the area of growth can be limited by selectively irradiating the sample [77]. By scanning the laser beam across a sample, patterns can be drawn onto the surface. Therefore, LCVD allows for growth and simultaneously patterning of materials on a substrate with lateral dimensions down to the submicron scale [76]. Another obvious advantage of LCVD over CVD is that the growth rates for LCVD are orders of magnitude faster than for traditional CVD [76]. Park et al. studied that graphene growth in LCVD is several thousand times faster than that in conventional CVD [35].

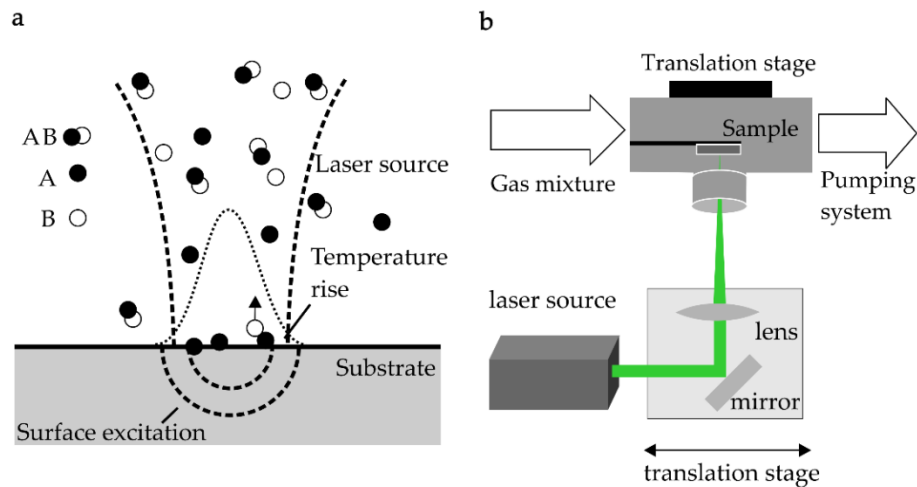


Figure 3. 4. a) Illustration of the LCVD process where the laser beam irradiates the substrate. A and B represent the molecules present in the chamber during the heating process of the laser beam [76]. b) Experimental setup of LCVD for direct laser writing of graphene. Fig. 2.4a is adapted from [76] and Fig. 2.4b is adapted from [78].

Fig. 3.4b shows the LCVD setup we used for this work. We employed a continuous-wave green laser (532 nm) as the heat source. By using a motorized stage, the laser scans over the sample. The sample itself sits in the vacuum chamber where the precursor gas is let in. The high temperature caused by the laser irradiation on the sample will initiate a dehydrogenation of the precursor, hydrocarbon gas [35]. Since the laser is moved across the sample, it is expected that lines of graphene will grow on the sample surface. A detailed explanation about our LCVD setup can be found in Chapter 4.

Chapter 4

Experimental Setup

This chapter discusses the LCVD system built during this work as well as the strategies to reach the primary objective of this research which was to grow graphene locally on Ni and Pt foils. There were three main steps to achieve that goal, building the LCVD system suitable for graphene growth, searching and optimizing the recipe for graphene growth on Ni foil by tuning the parameters of the LCDV system and implementing the optimized recipe for Pt foil. The first step is presented in subchapter 4.1, and the other two steps are presented in subchapter 4.2.

4.1. LCVD System

The LCVD system consists of a laser source, a scanning system, and a vacuum chamber (see Fig.4.1.a). The continuous-wave (CW) laser (optically pumped solid state laser; Coherent Co. G5) with $\lambda = 532$ nm is utilized as the heating source used in the experiments described here. The laser beam was aligned using an optical mirror and lens so that the incoming focused beam hits the sample perpendicularly. The beam path in this experiment is shown in Fig. 4.1a.

The optical mirror and lens used for aligning the beam were attached to a motorized stage that can be controlled using a computer. This system (a mirror, lens and motorized stage) served as the scanning system whose speed was able to be adjusted in the order of micrometer per second. The scanning direction is only in one direction (defined as x -direction in Fig 4.1a).

The chamber itself was made from stainless steel with a diameter of 4 cm and 12.5 cm length and was equipped with an aluminum bracket that holds the precursor gases (see Fig.4.1b). We employed CH_4 (Messer Methane 4.5 with purity of 99.995 %) and H_2 (Messer H_2 5.0 with purity of 99.995%) gas as the precursor gas. All gases were used without further purification. We utilized a mechanical valve (pressure reduction valve) as well as a needle valve to let each gas flow into the chamber and to control the partial pressure of each gas.

To control the position of the incoming beam relative to the sample, we utilized a translation stage attached to the chamber (see Fig. 4.1c). It can be moved manually in x , y , z directions by using three-micrometer screws. Thus, we can precisely move it together with the chamber on the micrometer scale (see Fig. 4.1c). We utilized a CCD camera to monitor the position of the beam spot on the sample before the experiment.

The chamber is connected to a turbo molecular pump with a rotary pump by means of flexible bellows. The bellows were intended to make the pump stay fixed while the chamber was moved.

The pumping system is situated at the side of the chamber opposite of the gas inlet pipe to ensure that the gasses pass over the sample.

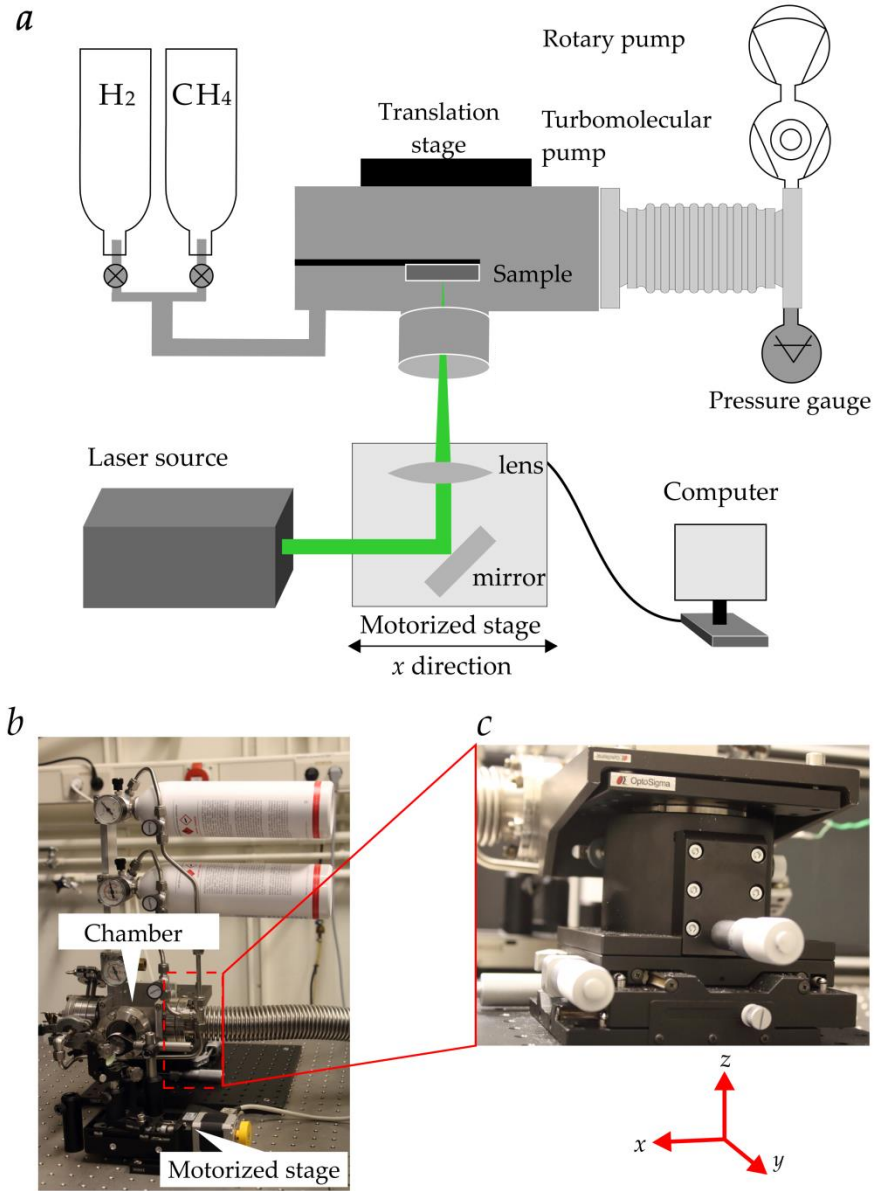


Figure 4. 1. a) Scheme of the LCVD system. The laser beam path is aligned by using a mirror and lens attached to a motorized stage. By moving the motorized stage in x direction using a computer, we are able to scan the laser beam on the sample. b) The home-built chamber is attached to the translation stage. This chamber is equipped with an aluminum bracket to hold the gas sources which are connected to the pumping system. c) The translation stage is controlled by a micrometer screw and can be moved in three directions (x, y, and z-direction).

Experimental parameters: There are six parameters in our experiment that can be tuned to control the graphene growth condition. Five of them are the parameters of the LCVD setup, which are the laser power, the beam diameter, the scanning rate, the partial pressure of gas mixture, and the base pressure. Another parameter is the type of material used as the substrate. In general, the temperature of the sample also depends on sample parameters (such as the type of material and the thickness), and the parameters of the laser, namely the laser power and the beam diameter [35, 36].

Two other tunable parameters were the base pressure of the chamber and the ratio of the gases in the mixture. Both were controlled by using the mechanical and needle valves attached to the chamber system. The pressure of the gas mixture was read by both Pirani and penning gauges connected to the pumping system.

4.2. Experimental Design of LCVD Graphene on Ni and Pt Foil

The two other steps to achieve the goal of this thesis are conducting a systematic study to obtain a recipe for growing graphene on Ni foil using LCVD, and implementing the recipe to Pt foil. To study LCVD graphene on Ni foil, we started the experiment based on the previous study of LCVD graphene on Ni foil done by Park et al [35]. The authors conducted the experiment with parameters summarized in Table 4.1. They used flowmeters to control the gas ratio and kept the total pressure at 500 torr (~666 mbar).

Our limitation in this experiment is that the laser power is maximum 4.5 watts and the beam diameter is around 30 μm . These numbers give a maximum intensity $\sim 10^5 \text{ W/cm}^2$ which is one order of magnitude lower than the intensity used by Park et al., $\sim 10^6 \text{ W/cm}^2$. To vary the intensity of the laser, we varied the laser power and kept the beam diameter constant. In practice, we did not vary the beam diameter in the experiment of LCVD graphene on Ni foil.

Table 4. 1. Parameters used by Park et al. to grow a line of graphene using LCVD technique

No	Parameter	Value
1	Ni thickness	25 μm
2	Laser type	continuous wave laser $\lambda=532 \text{ nm}$
3	Laser power	5 watts
4	Beam diameter	20 μm
5	Scanning rate	50 $\mu\text{m/s}$
6	Gas ratio	$\text{CH}_4 : \text{H}_2 = 2:1$
7	Base pressure	10^{-3} torr ($\sim 10^{-3} \text{ mbar}$)

We selected three different thicknesses of Ni foils which are 16 μm (purity of 99.5 %), 25 μm (purity of 99.99%), and 125 μm (purity of 99.95%). We conducted many experiments by varying the laser power, scanning rate, and gas mixture. We kept the base pressure at 10^{-3} mbar. The results suggested that the 25 μm Ni foil and 4.5 Watt laser were two important parameters to generate the graphene growth temperature.

We conducted experiments with 4 fixed parameters and 2 varied parameters. We used Ni foils with a thickness of 25 μm , the laser power of 4.5 Watts, the beam diameter of around 30 μm , and the base pressure of 10^{-3} mbar. We varied the gas mixtures and the scanning rates. It turned out that we had to lower the base pressure (see subchapter 5.1.2).

We conducted the further experiments under a base pressure of 10^{-7} mbar. We varied the gas mixtures and the scanning rates. The output of these experiments resulted in the recipe for graphene growth on Ni foil by using LCVD.

We applied the recipe that worked for Ni foil to Pt foil. We used Pt foil since it has similar properties with Ni regarding how it interacts with the laser. The parameters used in this experiment are: the laser power of 4.5 Watts, scanning rate of 50 $\mu\text{m/s}$, gas mixture of 6×10^{-3} mbar of CH_4 and 1×10^{-3} mbar of H_2 , foil thickness of 25 μm .



Figure 4. 2. Illustration of how the Raman measurements were performed on the samples. The laser of the Raman setup was moved slowly across the sample to find the desired signal. The red arrow illustrates the direction of the Raman laser while the black lines indicate the ‘invisible’ laser pathway.

The presence of graphene (and other materials grown on the sample) was analyzed using optical microscopy, Raman spectroscopy, and SEM. The optical microscope was used to detect the laser pathway resulted on the sample. However, changing some parameters in the experiments may cause the laser pathway to become invisible under the optical microscope. On the sample with visible laser pathways, Raman spectra were collected inside and around the laser pathway. However, the laser pathway in the experiments under a base pressure of 10^{-7} mbar was not so obvious (subchapter 5.1.3, 5.1.4, and 5.2). Thus, the Raman spectra were collected by moving the Raman laser across 'the laser pathways' on the samples (see Fig. 4.2). SEM characterization was used for supporting the data obtained by Raman spectroscopy. SEM characterization can be used to observe the morphology of graphene on Ni foil and on Pt foil.

Chapter 5

Results and Discussions

5.1. LCVD Graphene on Ni Foil

In this section, we summarize and discuss the results of the LCVD experiments on Ni foils. Six parameters were involved. They were the foil thickness, laser power, beam diameter, scanning rate, gas mixture, and base pressure. We conducted many experiments by varying parameters (except for beam diameter) to obtain the proper recipe to grow graphene. Each variation was assigned as one laser pathway on the foil.

Subchapter 5.1.1 discusses the results of experiments for thickness optimization. Subchapter 5.1.2 discusses the results of experiments by varying gas mixtures and scanning rates under a high base pressure. Subchapter 5.1.3 discusses the results of experiments by varying gas mixtures and scanning rates under a low base pressure. Subchapter 5.1.4 discusses the results of experiments for scanning rate optimization. It is noteworthy that there were no pretreatments for cleaning the sample preceding all experiments.

We started the experiment based on the previous study of LCVD graphene on Ni foil conducted by Park et al. [35] as stated in Chapter 4. Due to the limitation of our LCVD system, we utilized a laser with a maximum power of 4.5 watts and a beam diameter of around 30 μm . We kept the value of beam diameter throughout all experiments.

All samples were characterized by an optical microscope and Raman spectroscopy. The optical microscope was used to observe whether there is visual change due to a laser pathway on the sample after experiments were completed. The Raman spectroscopy was used to identify what material that formed on the sample. A SEM characterization was also used to observe the morphology of graphene (and other materials) on the sample. However, this SEM characterization was only performed for particular samples.

5.1.1. Thickness optimization

In this set of experiments, we used Ni foils with three different thicknesses, 16 μm (purity of 99.5%), 125 μm (purity of 99.95%), and 25 μm (purity of 99.99%). The base pressure was set at 10^{-3} mbar. The variations in these experiments are reported in Table 5.1. In total there were 90 laser pathways resulted in this set of experiments.

Table 5. 1. The variations of parameters in the thickness optimization experiment

Parameters	Variations
Thickness	<ul style="list-style-type: none"> - 16 μm - 125 μm - 25 μm
Base pressure	- 1×10^{-3} mbar
Gas mixture	<ul style="list-style-type: none"> - Gas mixture 1 (0.1 mbar of Ar, 0.5 mbar of CH_4, and 0.5 mbar of H_2) - Gas mixture 2 (2 mbar of CH_4 and 1 mbar H_2)
Laser power	<ul style="list-style-type: none"> - 1 watt - 2 watts - 3 watts - 4 watts - 4.5 watts
Beam diameter	- ~ 30 μm
Scanning rate	<ul style="list-style-type: none"> - 10 $\mu\text{m/s}$ - 20 $\mu\text{m/s}$ - 50 $\mu\text{m/s}$

The results were independent of the gas mixture and the scanning rate variations. Hence, the discussion is mainly focused on how the laser power and the thickness of Ni foil affect the temperature generated by the laser.

Figs. 5.1a show typical optical images of the 16 μm (top), 25 μm (middle), 125 μm (bottom) foils after the experiments were completed. The laser with a power of 2 watts or higher completely ablated the 16- μm foil (region A in top image). The rainbow-like color of the area under the foil belongs to the sample plate. There was also visual change around the ablated area (region B in top image). The sample exposed by 1-watt laser only changed its color like in region B. The laser with a power of 4.5 watts generated a laser pathway on the 25- μm foil (region C in middle image) and generated a shadow around the ablated area (region D in middle image). The 1-and 2-watt laser only generated a shadow on the sample while 3-to-4-watt laser generated a tiny laser pathway. The bottom image in Fig. 5.1a shows a typical image of the 125- μm foil after exposed to the laser. Regardless of the power used, the foil did not show any visual difference.

Figure 5.1b shows a typical Raman spectrum measured around the ablated area of the 16 μm foil (region B in Fig. 5.1a). Region A is not relevant since it is the sample plate. The Raman spectrum exhibits two high-intensity peaks located at 1368 cm^{-1} and 1400 cm^{-1} . There are also several small peaks compared to those two peaks, which are located at 1500 cm^{-1} , 1600 cm^{-1} , and 1800 cm^{-1} . This

spectrum is probably related to a hydrogenated amorphous carbon (mixing of sp^2 and sp^3 carbons with hydrogen) forming on the surface.

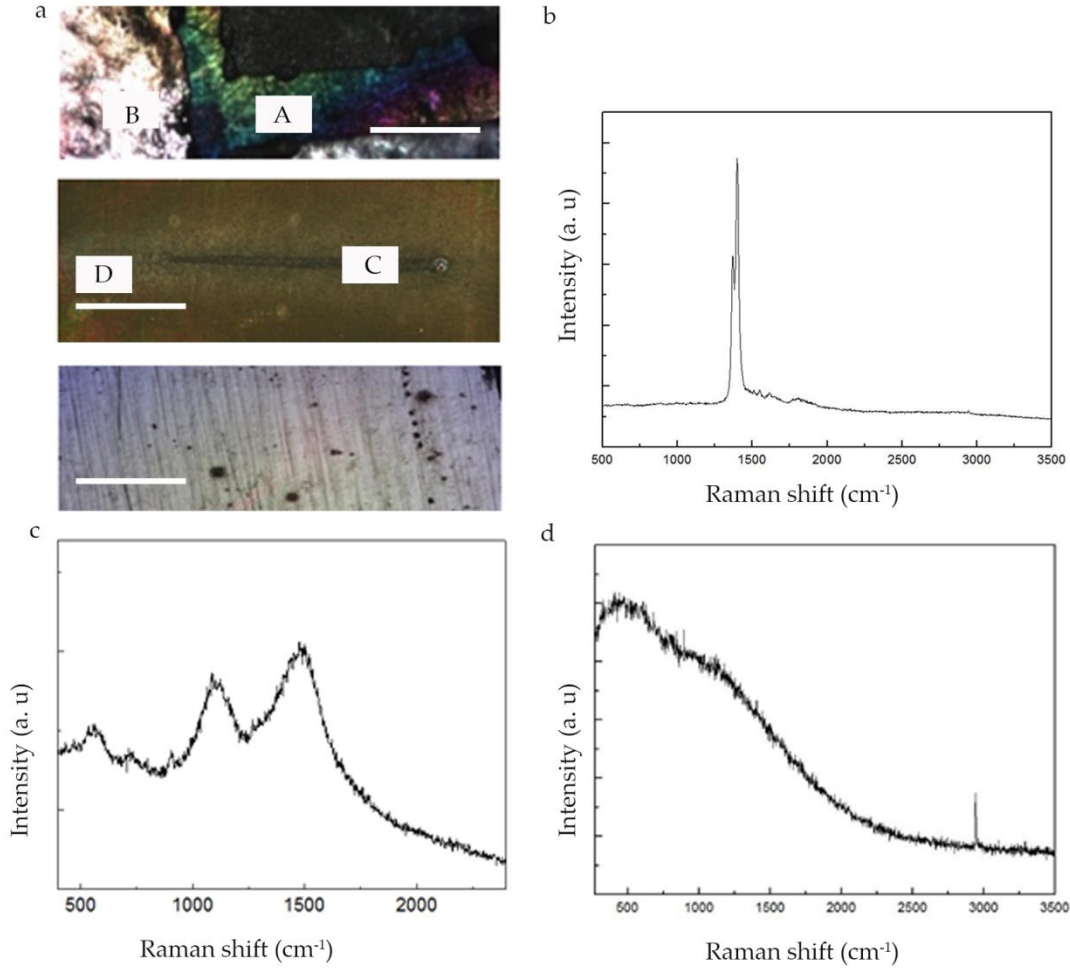


Figure 5. 1. a) Optical image (top) of Ni foil with 16 μm thickness exposed to the laser with a power of 2 Watts, optical image (middle) of Ni foil with 25 μm thickness exposed by the laser with a power of 4.5 Watts, and optical image (middle) of Ni foil with 125 μm thickness after exposed by the laser with a power of 4.5 Watts. b) Typical Raman spectrum that was measured around the laser pathway (region B) regardless the power, gas mixture, and scanning rate used in the experiments. c) Typical Raman spectrum that was measured either in the laser pathway (region C) or in the shadow (region D) of the 25 μm foil regardless the power, gas mixture, and scanning rate used in the experiment. d) Typical Raman spectrum of Ni foil with 125- μm thickness. The bar scale in the optical image is 100 μm .

There are two reasons for interpreting this spectrum as a hydrogenated amorphous carbon. The first reason is that we only used carbon precursor and hydrogen in our experiment. It is reasonable that we expect the formation of related carbon material is dominant on our sample.

Moreover, all carbon materials show common peaks in their Raman spectra in the 800- 2000 cm^{-1} region [79]. The peaks commonly shift due to the crystallinity, sp^2 : sp^3 content, and the excitation energy of the Raman laser. As it can be seen in Fig. 5.5d, the spectrum exhibits the peaks located in the 800 cm^{-1} - 2000 cm^{-1} region. The second reason is that Raman spectroscopy can be used to indirectly determine approximately the quantity of sp^2 phase and sp^3 phase in carbon materials. We expect that the peaks appear in the spectrum will relate to a combination of sp^2 and sp^3 carbon phase, which is a definition for amorphous carbon [79].

The two peaks at 1368 and 1400 cm^{-1} are probably due to a consequence of a lot of sp^3 contents on the sample. These peaks are related to CH_2 and CH_3 [80, 81] that may be bounded to sp^3 carbon. The sp^3 content is commonly achieved by H saturating C=C bonds as CH_x groups, rather than by increasing the fraction of C-C sp^3 bonds. Then, most of the sp^3 sites are bounded to hydrogen [82]. In a hydrogenated amorphous carbon, the sp^2 carbons can exist as rings or chains. Increasing H contents reduces the amount of sp^2 carbon rings. If there is no sp^2 carbon ring, the G peak and D peak will disappear [79]. In this spectrum, it may be that the amount of sp^2 carbon rings is little. Hence, the G and D peaks are almost invisible in this spectrum. The tiny peak at 1500 cm^{-1} can be assigned as the G peak subjected red-shift due to lack of sp^2 carbon rings [79].

Based on this interpretation the spectrum is most likely related to a hydrogenated tetrahedral amorphous carbon (ta-C: H). The ta-C: H is defined as an amorphous carbon that consists more sp^3 than sp^2 carbons. The peak located at 1600 cm^{-1} may be related to the appearance of sp^3 or due to C-H vibration in hydrogenated carbon [83] while the origin of a peak at 1800 cm^{-1} is not clear. The shape of the spectrum is narrower than that in the literature [84], but the peak at 1368 and 1400 fit with alkyl vibration [80, 81].

Fig. 5.1c shows the Raman spectrum measured inside the laser pathway (region C) and its surrounding shadow (region D) on the 25 μm -thick foil. There are four pronoun peaks located at 570 cm^{-1} , 710 cm^{-1} , 1100 cm^{-1} , and 1500 cm^{-1} . These peaks are a signature for nickel oxide [85] [86] [87] [88]. Sometimes, this spectrum was also detected in the foil with a thickness of 16 μm (in the area away from the melted area).

The corresponding Raman spectrum for the 125 μm -thick foil is shown in Fig. 5.1d. This Raman shape is the same as that of bare Ni foil (background spectrum). The feature at 2900 cm^{-1} is due to the Raman setup. This peak always appeared whenever the Raman laser was defocused on the sample. The background spectrum has a typical shape just shown in Fig. 5.5b. This spectrum is due to Raman setup and has nothing to do with the Ni foil. This is because this background will also appear to the other sample that is Raman inactive, typically for pure metal [89]. As we will see in subchapter 5.2, this background also appears when we collected the Raman spectra on Pt foil.

In the case of the 16 μm Ni foil exposed to the 2-watt laser, the amorphous carbon was found around the ablated area while NiO was found on the surface away from the ablated area. Since the foil was completely ablated, the temperature of the area under the beam must be above 1450 $^{\circ}\text{C}$ (the melting point of nickel) [90]. This temperature will diffuse and decrease as the distance increases from the ablated area [91]. The temperature of region B may be near the melting point of nickel while the temperature away from the ablated area may be lower than that of region B. We did not interpret the temperature of the 16- μm foil exposed to the laser with a power of 3, 4, or 4.5 Watts because it is clear that the temperature is too high for graphene growth. However, there can be a possibility to lower down the laser power to obtain the temperature of the graphene growth.

In the case of 25- μm Ni foil exposed to the 4.5-watt laser, NiO formed on every laser pathway resulted on the sample. Nickel can react with oxygen at a temperature of 400 $^{\circ}\text{C}$ and react with water at a temperature of 1000 $^{\circ}\text{C}$ to form NiO [92]. Several studies have shown that NiO can be reduced by CH_4 at the temperature around 600-725 $^{\circ}\text{C}$ [93, 94]. However, at temperature higher 900 $^{\circ}\text{C}$ the reduction of NiO by CH_4 decreases significantly [93].

Since we performed the experiments under a base pressure of 10^{-3} mbar, the residual gases may still exist in the chamber. The residual gases during a pumping down in the regime of medium vacuum (10^{-3} mbar) are dominated by water vapor. The water desorbs from the internal surface of the chamber. The water vapor absorbs and adsorbs on the internal surface of the chamber during loading the sample [95, 96]. The temperature may be around 1000 $^{\circ}\text{C}$, at which the water can react with Ni to form a significant amount of NiO. At that temperature, CH_4 can reduce NiO. The ablated part in the laser pathway is most probably due to NiO that is partially reduced by CH_4 . This is evident because the Raman spectra collected from the laser pathway (ablated part) and the shadow show the presence of NiO.

It is hard to analyze what the temperature was on the 125- μm foil exposed to the laser since there is no visual change in optical image and no change in Raman spectrum. It can be concluded is that there are no carbon materials that can be observed by Raman spectroscopy on this sample. Thus, it is not reasonable to have this sample for further experiments.

Due to this temperature interpretation, it is most probably that 25 μm is appropriate thickness for the next experiment. This foil is not too thin as the 16 μm foil that could damage under low-power laser (2 watts) and not too thick as the 125 μm foil that presumably cannot generate high enough temperature for the dehydrogenation process. Furthermore, a typical temperature for growing graphene on Ni foil is around 900 $^{\circ}\text{C}$, even lower [69], which is most likely generated on the 25 μm foil.

5.1.2. Gas mixture and scanning rate variation under a high base pressure

It was suggested that the 25- μm Ni foil exposed to 4.5-watt laser generates temperature that is presumably around 1000 $^{\circ}\text{C}$. We used these two parameters (thickness and laser power) in this set of experiments. We kept the base pressure at 10^{-3} mbar. We previously varied the gas mixture and scanning rate. However, we only varied 2 gas mixtures. We varied more gas mixtures in these experiments to justify the result in the previous experiments. The gas mixtures for this set of experiments are reported in Fig. 5.2 while the variation of the scanning rate is 10, 20, and 50 $\mu\text{m/s}$. On the sample with each mixture, we scanned the lines with three different scanning rates (three lines per sample).

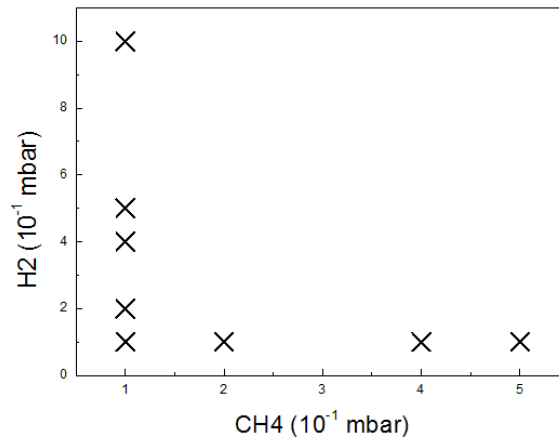


Figure 5. 2. The gas mixture variation used in the experiments under a base pressure of 10^{-3} mbar.

The results are independent of the gas mixture. Fig. 5.3 (a-c) shows the typical optical images of Ni surface after the experiments were completed. The scanning rates of 10 $\mu\text{m/s}$, 20 $\mu\text{m/s}$, and 50 $\mu\text{m/s}$ resulted in the laser pathways with the width of around 50 μm (see Fig. 5.3a), 40 μm (see Fig. 5.3b), and 30 μm (see Fig. 5.3c), respectively. It can be seen that the width of the laser pathway is smaller as the scanning rate increases.

Raman spectra were collected inside and around all laser pathways. The results show a typical Raman spectrum as depicted in Fig. 5.3d. The Raman spectrum exhibits two sharp peaks at 560 and 710 cm^{-1} and two broader peaks at 1100 and 1500 cm^{-1} . These peaks are signatures for NiO. This spectrum is similar to that measured in the previous experiments with 25 μm thickness foils. However, the characteristic peaks at 560 and 710 cm^{-1} have a higher intensity than that in the previous experiment (see Fig. 5.1c). Even though it is interesting to investigate the origin of this intensity, it is beyond our study. We only recognize that the peaks in the spectrum originate from NiO [85].

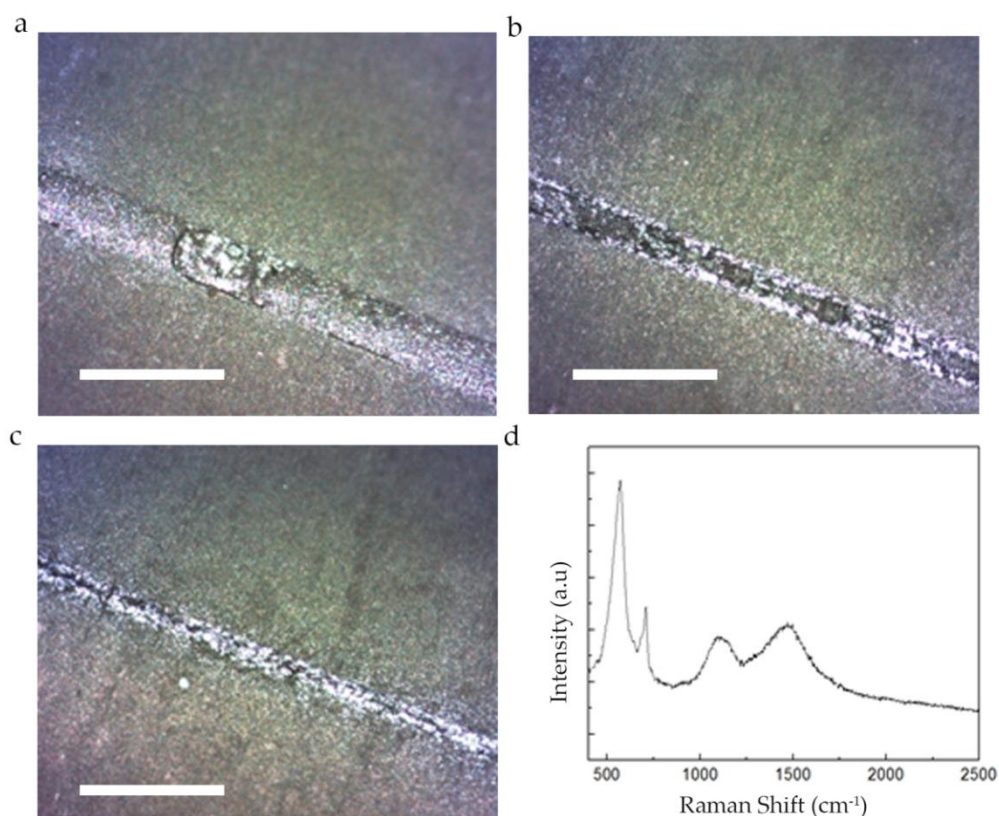


Figure 5. 3. Optical image of Ni foil with 25 μm thickness exposed to the laser at a power of 4.5 Watts with a scanning rate of a) 10 $\mu\text{m/s}$, b) 20 $\mu\text{m/s}$, and c) 50 $\mu\text{m/s}$. All samples with variations of the gas mixture showed these typical images. d) A typical Raman spectrum measured inside the line regardless the gas mixture and the scanning rate used in the experiment. The scale bar in each optical image is 100 μm .

This Raman spectrum indicates that a significant amount of NiO was forming on the surface while the sample was exposed to the laser. As it was suggested in subchapter 5.1.1, the temperature on the μm Ni foil may reach around 1000 C due to the laser with abovementioned parameters. It may be expected that at that high temperature, the CH_4 will dehydrogenate on the Ni surface [97]. If CH_4 dehydrogenated, it should be carbon materials detected by Raman spectrum because the result of dehydrogenation contains carbon. However, such process was not indicated in the Raman spectra measured for all samples.

The NiO reduction by CH_4 depends on the amount of CH_4 and the reduction time [93]. The reason for having NiO spectrum on the samples may be that the amount of CH_4 is not enough to reduce NiO completely, or the reduction time is too short. The variations of the gas mixture did not give significant change because the total pressure of every gas mixture is in the same order of

magnitude, which is 10^{-1} mbar. This probably does not give a significant difference in the amount of CH_4 to reduce NiO. Furthermore, the scanning rates were also in the same order of magnitude so that there is no significant change in reduction time. Thus, all variations in this experiment resulted in a typical Raman spectrum depicted in Fig. 5.3d.

The formation of NiO is most likely due to the residual gas inside the chamber as discussed in subchapter 5.1.1. There are several ways to lower down the residual gas, such as baking the system or increasing the pump speed [96]. We see that increasing the pumping speed and pumping down the system at a base pressure of 10^{-7} mbar is the efficient way. Thus, the follow-up experiment was carried out under a base pressure of 10^{-7} mbar reducing the contaminants.

5.1.3. Gas mixture and scanning rate variation under a low base pressure

A set of experiments was performed on the 25- μm Ni foils by varying the CH_4 and H_2 mixtures and the scanning rate. We used 8 mixtures reported in Fig. 5.4. The variations of the scanning rates are 10, 20, and 50 $\mu\text{m/s}$. The growing experiments were performed by using a laser power of 4.5 watts and under a base pressure of 10^{-7} mbar. For each foil, we used one mixture and scanned 6 lines consisting of 2 lines of 10 $\mu\text{m/s}$, of 20 $\mu\text{m/s}$, and of 50 $\mu\text{m/s}$.

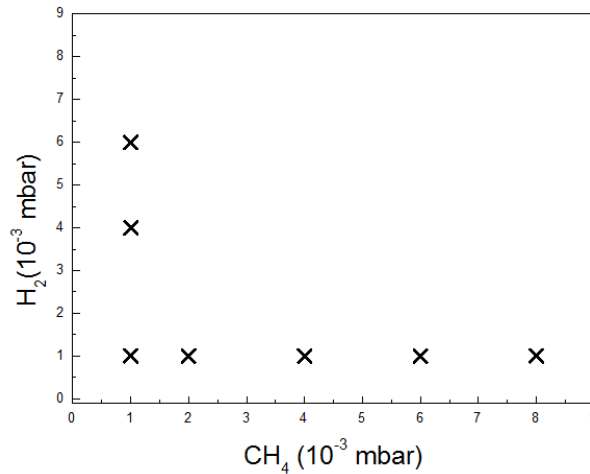


Figure 5. 4. The gas mixture variations used in the experiments under a base pressure of 10^{-7} mbar.

A typical optical image for all samples after the experiments were completed is depicted in Fig. 5.5a. In this figure, the laser pathway (see the dashed line) is assigned by the cracks. We cannot determine precisely where the inside or outside of the laser pathway. Therefore, we collected the Raman spectra by moving the Raman laser slowly across the sample. A consequence of this method is that we cannot determine which Raman spectrum comes from which scanning rate. Hence, we only see the influence of gas mixtures on the formation of graphene on the 25- μm Ni foil. Three typical Raman spectra of all samples are reported in Figs. 5.5 (b-c).

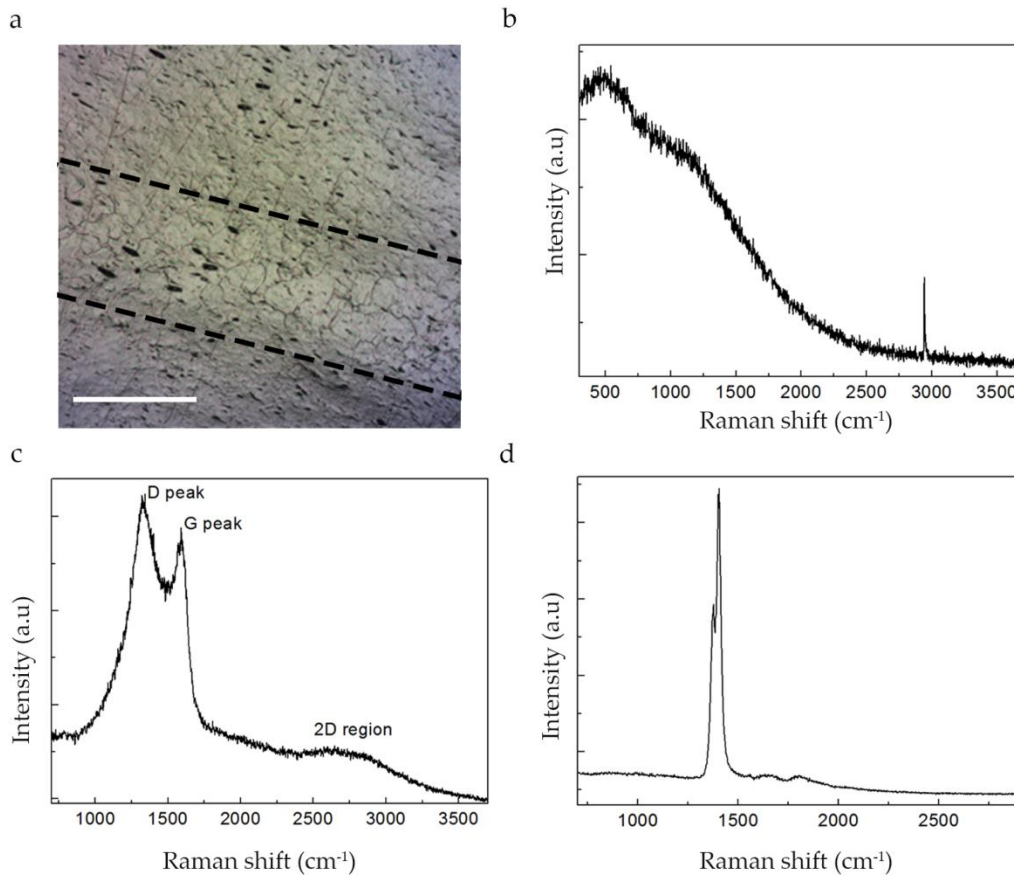


Figure 5.5. a) A typical image of the samples under a base pressure of 10^{-7} mbar. The scale bar is 100 μm . The three typical Raman spectra observed on each foil are b) the background spectrum, c) a typical spectrum for MLG (showing D band; 1340 cm^{-1} , G; 1583 cm^{-1} band and 2D-band region) and d) the spectrum related to ta-C: H.

The spectrum depicted in Fig. 5.5b is the background spectrum of Ni foil. The feature at 2900 cm^{-1} is due to the Raman setup. In the spectrum depicted in Fig. 5.5c, two intense peaks are the D peak at 1340 cm^{-1} and G peak at 1583 cm^{-1} while a modulated bump region from 2350 to 3250 cm^{-1} is designated as a 2D region. This spectrum could be assigned as multilayer graphene (MLG) which will be discussed below. The spectrum shown in Fig. 5.5d is the ta-C: H spectrum (as discussed in Subchapter 5.1.1).

The justification of MLG spectrum is due to the appearance of the G, D, and 2D (bump) peaks. The G peak is observed in the Raman spectrum of any number of graphene layers at $\sim 1590 \text{ cm}^{-1}$ and is related to the in-plane stretching of the C-C bonds. Even though the band position is independent of the laser's wavelength, it is highly sensitive to the number of layers of graphene. As the number of layers increases, the G band position shifts to lower energy representing a slight softening of the

bonds with each addition of graphene layer [98, 99]. It can be seen that the spectrum in Fig. 5.5c shows a shift of G band into 1583 cm^{-1} .

When the periodic lattice of graphene is broken by defects, the Raman spectrum exhibits a new peak at approximately 1350 cm^{-1} (514 nm laser) as D peak. This peak is dispersive. Hence, its actual positions depend on the laser wavelength. For 633 nm laser, the D peak appears at $\sim 1340\text{ cm}^{-1}$, which corresponds to our measurement. The high density of defects will disturb the hexagonal network of graphene, which may result in broadening in the FWHM of all peaks of D, G, and 2D. The broadening of D and G peak may lead into overlapping of these two peaks [79], like in our spectrum. This consequence was also studied by Ferreira et al. who have shown that the broken network of graphene causes the broadening of 2D peak [100]. Kaniyoor et al. have shown a similar bump of the 2D band. They addressed that bump as a consequence of wrinkled MLG. The wrinkles are generated by a high density of defects [83]. Hence, it is most probably that the spectrum shown in Fig. 5.5c is related to the wrinkled MLG (in this thesis we refer MLG to this wrinkled MLG).

The spectrum shown in Fig. 5.5d is a typical spectrum that was also found in the $16\text{ }\mu\text{m}$ foil in the initial experiment (see Subchapter 5.1.1). We already interpreted that this spectrum may be related to ta-C: H that may present around the MLG flakes. This typical spectrum was frequently recorded next to the area where the MLG spectrum was recorded. The morphology of this amorphous carbon and MLG graphene grown on Ni foil by using LCVD is given in the SEM image which will be discussed in sub-chapter 5.1.4.

Table 5. 2. The number of MLG spectra and amorphous carbon spectra recorded from all samples.

No	Gas ratio (CH ₄ :H ₂)	Number of MLG spectra	Number of ta- C:H spectra
1	1 to 6	3	5
2	1 to 4	1	5
3	1 to 1	3	5
4	2 to 1	3	6
5	4 to 1	6	2
6	6 to 1	9	2
7	8 to 1	0	7

All samples have shown the MLG spectra except for the sample with a gas mixture of 8×10^{-3} mbar of CH_4 and 1×10^{-3} mbar of H_2 . In this sample, all recorded spectra are related to ta-C: H. Other mixtures can be used to form MLG on the 25- μm Ni foil by using LCVD technique. It can be seen in Table 5.2 that the spectrum of MLG was measured on the samples with those recipes. However, the number of MLG spectra measured varies with the recipes. The formation of MLG is less than that of ta-C: H in the recipe 1-4. However, in the recipe 5 and 6, there are more MLG spectra than ta-C: H spectra. The recipe 5 and 6 give the optimum results regarding the number of MLG spectra. The MLG spectra are found on many spots of the samples with these two recipes. However, the number of MLG spectra measured on the sample is not related to the quality of MLG. For recipe 1 until 6, the quality of MLGs in these experiments are the same.

The factor determining the different number of MLG spectra from each sample was not clear. It could be the gas mixture or the scanning rate. The gas mixture provides a number of carbons dissolving into bulk, and the scanning rate ruled the heating time. Both quantities, a number of carbons and the heating time, determine the quality of graphene [65, 97] [97]. Changing the gas mixture may lead to a different optimum scanning rate. Furthermore, on each sample, we cannot decide which laser pathway (with specific scanning rate) contributes to the MLG spectrum. Nevertheless, based on the results of these experiments, we could infer that MLG can grow on Ni foil with 6 variations of the gas mixture.

In order to narrow down the optimized recipe, we chose one gas mixture, 6×10^{-3} mbar of CH_4 and 1×10^{-3} mbar of H_2 , which gave the largest number of MLG spectra because we can expect that those spectra came from all laser pathways on the sample, meaning all scanning rates contribute to MLG spectra. We would like to see further the optimization of the scanning rate on one mixture.

5.1.4. Scanning rate optimization

The successive experiments were to investigate the influence of the scanning rate on the MLG growth. The mixture of 6×10^{-3} mbar of CH_4 and 1×10^{-3} mbar of H_2 was chosen. The growing experiments were performed by using a laser power of 4.5 watts and under a base pressure of 10^{-7} mbar. The variations of the scanning rate were 10, 20, 50, 100 and 200 $\mu\text{m/s}$. For each sample, we scanned 6 lines with the same scanning rate. Therefore, even though we did not see laser pathways, we can assign a spectrum to a specific scanning rate.

As expected, the three typical spectra discussed in Subchapter 5.1.3 (Fig. 5.5b, c, and d) were also observed in this set of experiments. The background spectrum, the MLG spectrum, and the ta-C:H spectrum are depicted in Fig. 5.6 (a-c). However, another typical spectrum was also observed (see Fig. 5.6d). This spectrum exhibits several peaks located at 1180 cm^{-1} , 1242 cm^{-1} , 1368 cm^{-1} , 1400 cm^{-1} ,

and 1500 cm^{-1} . This spectrum may relate to another kind of amorphous carbon, which is hydrogenated amorphous carbon (a-C: H).

The peaks of the spectrum shown in Fig. 5.6d could be assigned as the following. The peak located at 1500 is the G peak that related to the sp^2 carbons in the sample. This peak shift into lower wavenumber due to decreasing the size of sp^2 carbon ring [79]. The sp^3 contents make defect in the sp^2 cluster. Most of the sp^3 carbon may be bonded to hydrogen because the spectrum shows the same peak as ta-C: H (see Fig. 5.6c). The D band may occur at 1340 cm^{-1} , but it is hidden under the shoulder next to the peak of 1242 cm^{-1} . The peak at 1180 may originate from microcrystalline sp^3 carbon [101] while the peak at 1242 cm^{-1} could originate from the presence of distorted sp^2 bonds (nonhexagonal rings) [102]. This spectrum could be related the presence of hydrogenated amorphous carbon (a-C: H) which still has sp^2 carbon rings proven by the presence of G (and D) peak.

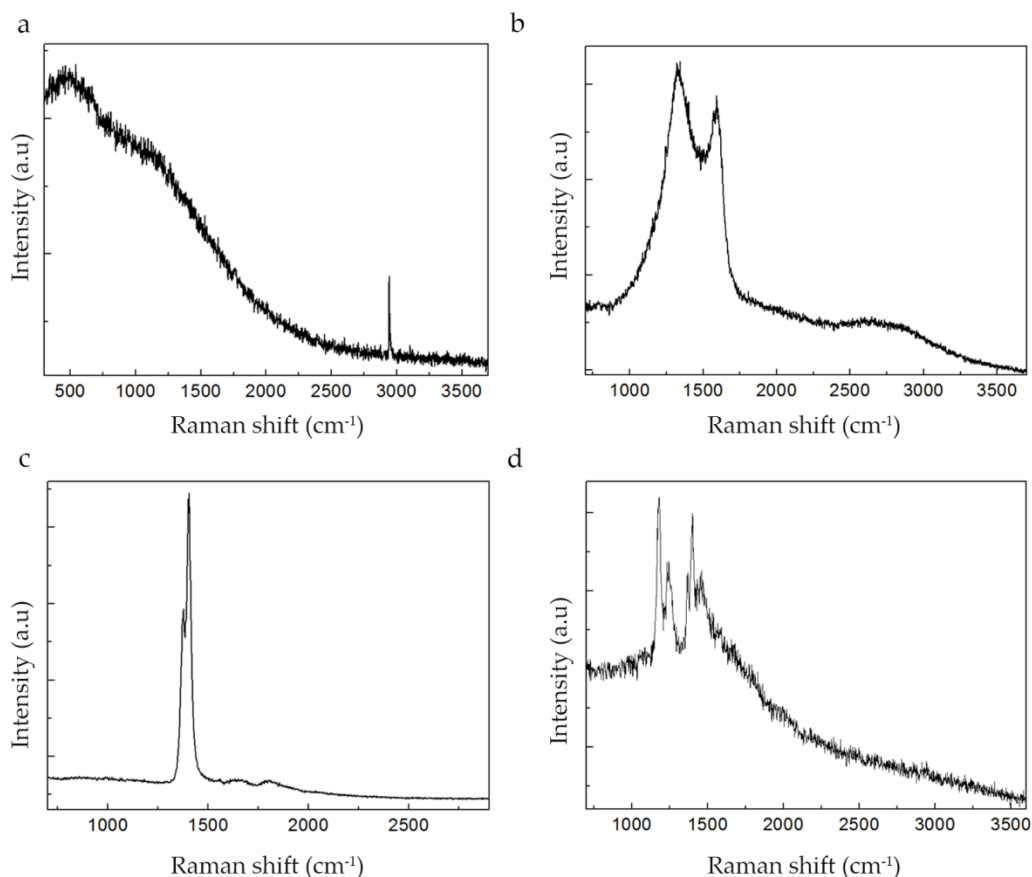


Figure 5. 6. The four typical spectra observed are a) the background spectrum, b) MLG spectrum, c) ta-C: H spectrum, and d) a-C: H spectrum.

Table 5. 3. The number of MLG, ta-C: H, and a-C: H spectra from all samples.

No	Scanning rate ($\mu\text{m/s}$)	Number of MLG spectra	Number of ta-C:H spectra	Number of a-C:H spectra
1	10	3	5	0
2	21	5	6	0
3	50	7	2	1
4	100	0	6	1
5	200	0	3	1

It can be seen from Table 5.3 that the MLG spectra were observed in the sample with scanning rates of 10, 20, and 50 $\mu\text{m/s}$ while the sample with scanning rates of 100 and 200 $\mu\text{m/s}$ did not show the MLG spectrum. Instead, only two kinds of amorphous carbons were observed on the samples with scanning rates of 100 and 200 $\mu\text{m/s}$. Perhaps, when the laser moved with a scanning rate of 100 $\mu\text{m/s}$ or faster, the heating time is too fast. There is not enough time for carbon atoms to form ordered structure completely [103]. The carbons may end up with a finite size of graphitic crystal bounded to large amount of sp^3 carbons.

The SEM image of the sample with 50 $\mu\text{m/s}$ scanning rate is shown in Fig. 5.7a. This image was measured on the very edge of the sample (edge of the laser pathway). It can be seen that there are three regions (region A, B, and C) covered by this image. These regions were not observed under an optical microscope. We can infer that the flakes may indicate graphene and amorphous carbon flakes. This image gives a supporting data for the obtained Raman spectra. The region A relates to the laser pathway on the sample. This pathway appears as the brightest contrast with flakes. The region B shows darker contrast than that of region A and also shows drifting lines. The region C is the bare Ni foil.

The flakes on the region A can be seen clearly in the zoom-in image depicted in Fig. 5.7b. It shows many domains of flakes. There are wrinkles on the bright flake that indicate the wrinkled film. This wrinkled film seems overlapping to some flakes with a darker contrast. The wrinkled film may indicate the MLG [104].

The zoom in the image of the region B is depicted in Fig. 5.7b. In this image, there are drifting lines like in zoom-out SEM image (see Fig. 5.7a). It means that the lines came from the material imaged. These drifting lines are commonly due to a charging problem, which means that the material

emits less secondary electron to produce the image. This problem commonly happens in non-conductive materials [105]. Due to this problem charging, this image may show the ta-C: H since it is a non-conductive material. The image of bare Ni foil can be clearly seen in Fig. 5.7c.

In the SEM image, the flakes of MLG are found along the laser pathway. This pathway is larger than the beam diameter of the laser. The pathway has a width of around 400 μm , which is larger than the diameter of laser beam spot of around 30 μm . The laser pathway enlarges due to the thermal diffusion in the sample. This enlargement is also followed by region B that may have a lower temperature during laser heating. It can be explained that the temperature, generated on the 25- μm Ni foil by a 30- μm focused laser with 4.5 watts, diffuse through the surface. The highest temperature should be in the center, under the laser beam and rapidly diffuse through the sample [91]. This different temperature may cause different grown material as indicated by Raman measurement.

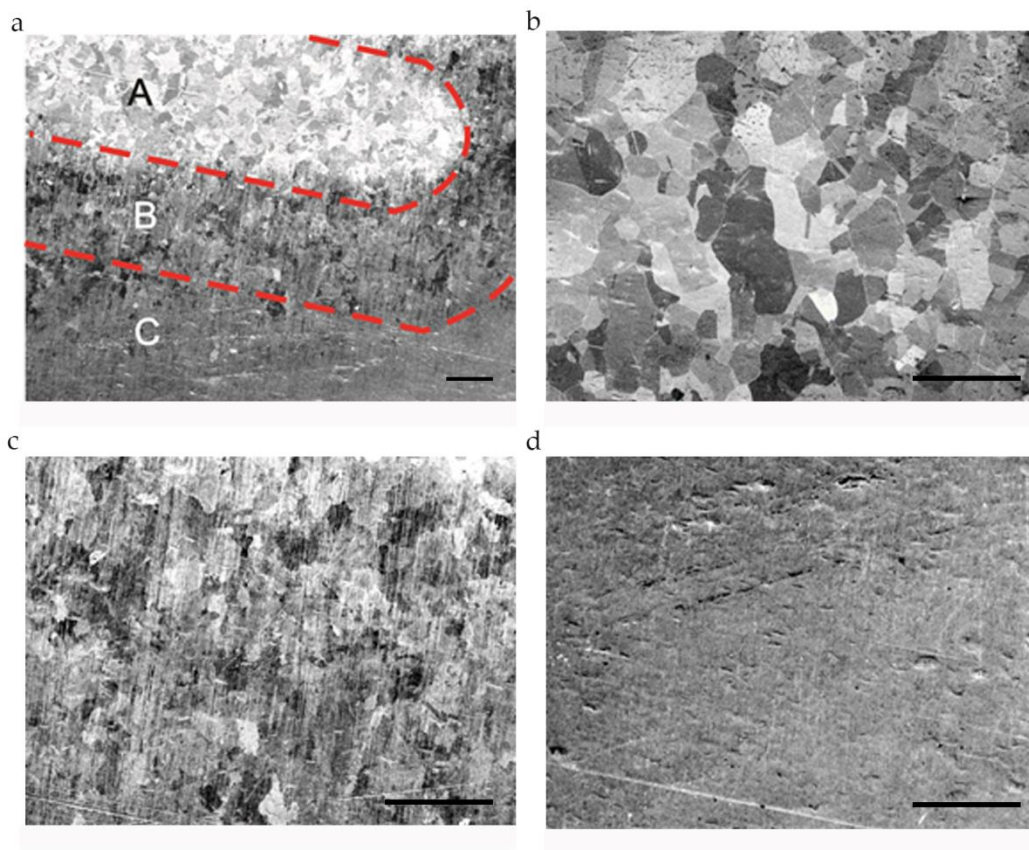


Figure 5. 7. a) SEM image of MLG flakes grown on Ni foil by using a gas mixture of 6×10^{-3} mbar of CH_4 and 1×10^{-3} mbar of H_2 and the scanning rate of 50 $\mu\text{m}/\text{s}$. The laser pathway is shown as the region A. It can be seen clearly the border between the line and its surrounding. b) The zoom-in image of the region A, c) region B, and d) region C which is the bare Ni foil. The scale bar in each figure is 100 μm .

In general, the results of LCVD graphene on Ni foils differ from that obtained in the work of Park et al. [35]. The authors showed the high-quality graphene grown with similar technique after many trials. They used continuous wave green laser with a power of 5 Watts and a scanning rate of 50 $\mu\text{m/s}$. The laser beam was focused around 20 μm , and the gas mixture ratio is 2:1 for CH_4 : H_2 . They used a flow meter to control the gas ratio while we used a reducing valve to control the gas mixture. These different tools may result in different growth condition and generate different results. They also showed that the line width of the laser pathway is around 10 μm . It differs from our work that indicates the broadening in the laser pathway up to several hundred from the center of the line. They used 5 watts and 20 μm beam diameter that means the intensity is around 10^6 W/cm^2 , larger than our intensity which is 10^5 W/cm^2 . Even though we used the same sample but with different intensity will lead different temperature. Their result shows that they grow near the melting point which can be seen from their optical image. This condition differs from ours

Another study for LCVD graphene on Ni was done by Jiang et al. [36]. The authors used LCVD technique by using a 500-Watt infrared laser. They used the laser with a beam diameter of 1 mm. They showed that the laser pathway enlarged to 1.5 mm. Their results suggested that they can grow few layer graphene on the sample. Since the laser type also plays a role to determine the thermal diffusion behavior, so that we cannot compare the diffusion behavior with their work.

5.2. LCVD Graphene on Pt Foil

Based on the results of LCVD graphene on Ni foil, MLG can grow on Ni foil using LCVD with certain parameters. In the subchapter 5.1.4, the most promising recipe to grow graphene (showing many MLG spectra) is the following. The foil thickness is 25 μm . The base pressure is 10^{-7} mbar and the gas mixture is of 6×10^{-3} mbar of CH_4 and 1×10^{-3} mbar of H_2 . The laser is operated at 4.5 watts with a scanning rate of 50 $\mu\text{m/s}$. The beam diameter of the laser is focused on 30 μm .

Since this set of parameters works to grow MLG graphene on Ni foil, it should also work on the material having similar properties with Ni. The material that has a similar solubility of carbon with Ni will give the advantage to mimic the recipe. Another consideration is that the temperature generated on the material should be similar to that on Ni foil, by using the abovementioned LCVD parameters. The temperature of the sample irradiated by a laser depends on the following parameters; the heat capacity, the density, the thermal conductivity, the absorptivity to the laser, and the emissivity [91]. We decided to apply the recipe to Pt foil.

Platinum foil with a thickness of 25 μm (99.9% pure) was used in this experiment. The LCVD parameters used is mentioned above. The presence of graphene on this substrate was characterized by using Raman spectroscopy and SEM. The optical image was used to look whether the laser pathway is visible.

The optical image of Pt foil after LCVD experiment is depicted in Fig. 5.8.a. There is no visual change on the Pt surface, i.e. the appearance of Pt foil after LCVD process is similar to that of a bare Pt foil. The color contrast in the image is due to the camera and not due to the sample. On this Pt foil, we cannot make a determination of the laser pathway by an optical microscope. Therefore, we collected the Raman spectra by moving the Raman laser slowly across the sample just like in the case of Ni foil.

The resulted spectra are depicted in Fig. 5.8 (b-c). They are background spectrum, MLG spectrum, and ta-C:H spectrum. The MLG spectrum exhibits the D peak located at 1340 cm^{-1} , G peak at 1583 cm^{-1} and 2D region from the region from 2350 to 3250 cm^{-1} . The ta-C: H spectrum also shows typical features like in the ta-C: H spectrum on Ni foil. The MLG spectrum was observed more frequent (5 times) than the ta-C: H spectrum was (once).

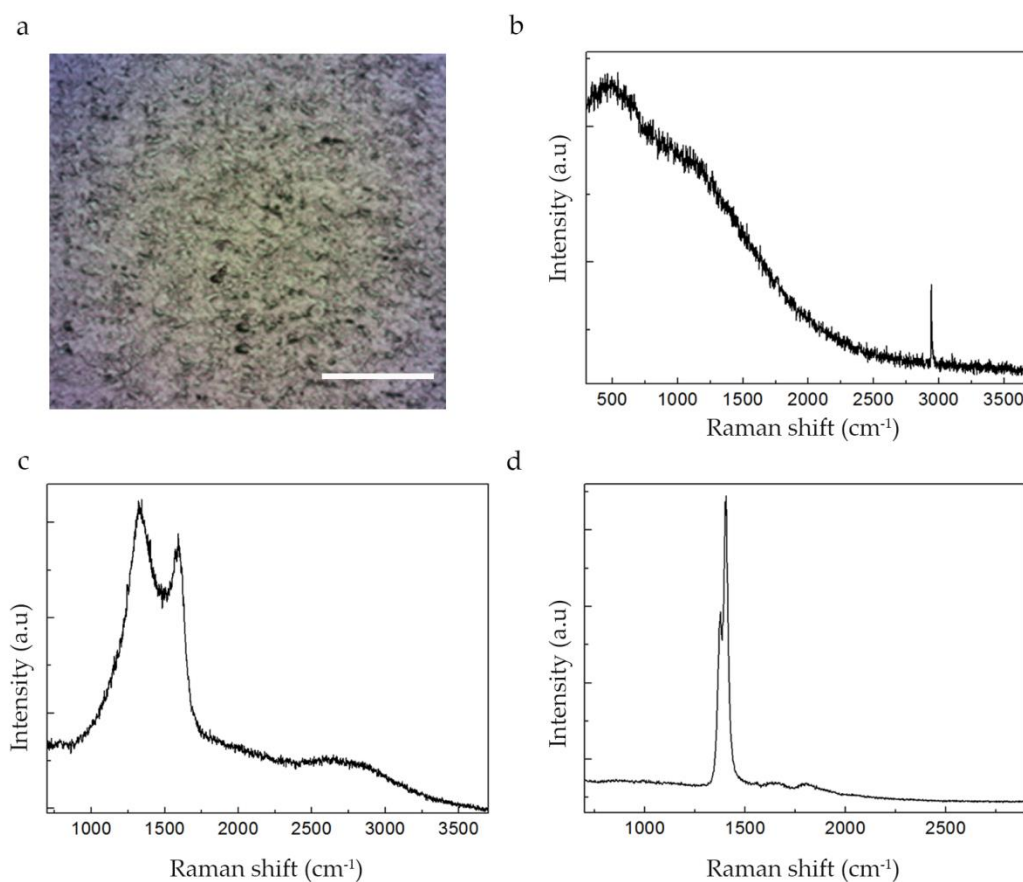


Figure 5. 8. a) A typical optical image of Pt foil after LCVD experiment was completed. The scale bar is $100\text{ }\mu\text{m}$ The three typical spectra observed in the Raman measurement are b) the background spectrum, c) typical spectrum for MLG and d) the spectrum related to ta-C: H.

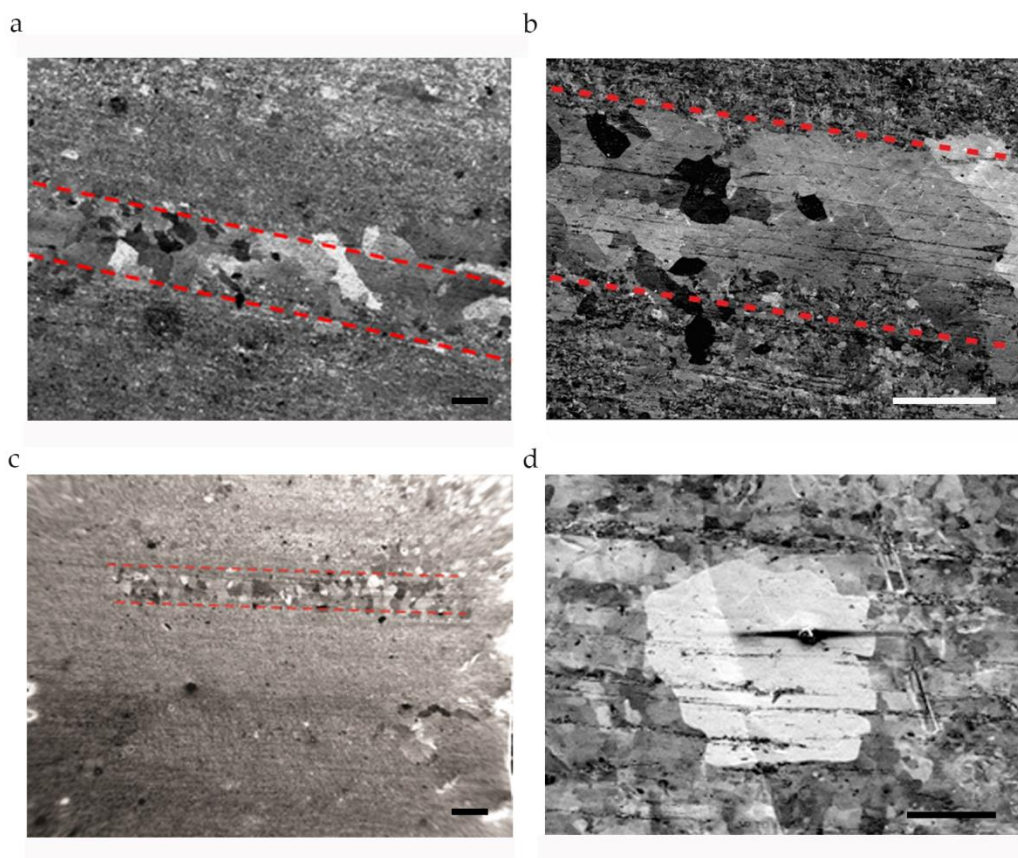


Figure 5. 9. a) SEM image of multilayer graphene flakes grown on Pt foil with a recipe of 6 to 1 ratio of methane and hydrogen and the scanning rate was 50 $\mu\text{m/s}$. The laser path is shown as domains of graphene flakes. The scale bar is 100 μm b) The zoom-in image of the line. There were domains and a wrinkled sheet of graphene flakes. The scale bar is 100 μm . c) SEM image of another laser pathway on Pt foil, indicated by the dashed line. The scale bar is 200 μm d) The zoom-in image of the line area shows one isolated flake of graphene. The scale bar is 10 μm .

Fig. 5.9a shows SEM image of the line consisting of MLG grown on Pt foil. The laser pathway is observed under SEM but not under the optical microscope. The width of the laser pathway is around 200 μm , which is smaller than that on Ni foil (see Fig. 5.7a). Furthermore, in Pt foil, the border between the line and the bare Pt is well defined due to localized heat generated by the laser. The heat on Pt foil is more localized than that on Ni foil because the heat on Pt foil diffuses slower than that on Ni foil. This is because the thermal conductivity of Pt foil is lower than that of Ni foil [106].

The zoom-in image inside the line is depicted in Fig. 5.9b. It can be seen clearly the wrinkled MLG sheet. The wrinkled in the edge can also indicate the presence of graphene [104]. It can be seen that the brighter film is wrinkled on top of some material with a darker contrast that may indicate as amorphous carbon. The SEM image of another MLG line grown on this sample is depicted in Fig.

5.9c. In this line, the isolated flake of one-domain graphene is observed (depicted in Fig. 5.9d) on top of wrinkled MLG. The observation of a single domain graphene on a wrinkled graphene sheet is typical on Pt foil. The study of graphene growth mechanism on Pt foil suggested that wrinkled MLG grows from below already deposited single layer [72].

To conclude, we manage to grow MLG on Pt foil by using LCVD technique. The same recipe used for graphene growth on Ni foil works for Pt foil. The morphology of MLG on Pt foil is more clearly seen than that on Ni foil. Furthermore, the isolated single domain graphene was also observed on Pt foil.

Chapter 6

Conclusions and Outlook

6.1. Conclusions

In this thesis, we built a homemade LCVD chamber for rapid synthesis of graphene line pattern. The system has tunable parameters that influence the graphene growth on the sample. Those parameters are the laser power, the beam diameter, the scanning rate, the partial pressure of gas mixture and the base pressure. In LCVD process, the material used as the substrate plays a significant role to determine the induced temperature. Different materials may generate different temperature when exposed to the laser with same parameters (power, beam diameter, and scanning rate).

We use Ni foil as the substrate for graphene growth using LCVD. In this thesis, we presented that the laser power (with fixed beam diameter) and the foil thickness need to be tuned to generate high temperature. In our LCVD system, the laser has a maximum power of 4.5 watts, and minimum beam diameter is 30 μm . It means the laser intensity has maximum value around 10^5 W/cm^2 . In order to generate temperature for graphene growth (around 800-1000 $^\circ\text{C}$) with this intensity, the thickness of Ni foil was chosen as 25 μm . However, these parameters (laser intensity and the foil thickness) are not absolute. One can tune these parameters to achieve the desired temperature.

In our system, the oxidation due to residual gasses was not prevented by setting a base pressure of 10^{-3} mbar (see discussion in sub-chapter 5.1.2). By using 4.5-watt laser and beam diameter of 30 μm , NiO was always observed inside and around the laser pathway, regardless the gas mixture and scanning rate used. In order to reduce the formation of NiO due to the residual gasses, we lower the base pressure down to 10^{-7} mbar.

We managed to grow a wrinkled MLG on the 25 μm Ni foil with parameters; the laser power of 4.5 watts, the beam diameter of 30 μm , the base pressure of 10^{-7} mbar and a range of $\text{CH}_4\text{-H}_2$ mixtures (presented in Fig. 5.4) and a range of the scanning rate (10, 20, 50 $\mu\text{m/s}$). The results were confirmed by Raman spectroscopy. The MLG growth was followed by the growth a hydrogenated tetrahedral amorphous carbon (ta-C: H) that consists of more sp^3 carbon than sp^2 carbon. This amorphous carbon most likely gives the defects for MLG on the sample.

We have investigated the variation of scanning rates (from 10 to 200 $\mu\text{m/s}$) on the sample with a mixture of 6×10^{-3} mbar of CH_4 and 1×10^{-3} mbar of H_2 . The MLG can grow on the sample scanned

by the laser with scanning rates of 10, 20, 50 $\mu\text{m/s}$ but not on 100 and 200 $\mu\text{m/s}$. The ta-C: H was found on all samples. However, on the samples with scanning rates of 50, 100, 200 $\mu\text{m/s}$, we found another type of amorphous carbon that consists more sp^2 rings than ta-C: H does. This carbon material is hydrogenated amorphous carbon (a-C: H).

The formation of a wrinkled MLG on the sample with a scanning rate of 50 $\mu\text{m/s}$ was confirmed by both Raman spectrum and SEM image. The SEM image shows that the laser pathway is not as large as the beam diameter. The width of the laser pathway is around 400 μm (see Fig. 6.1a). This enlargement of the pathway is due to thermal diffusion on Ni foil. The region B in Fig. 6.1a is probably amorphous carbon while the region C is bare Ni foil. The wrinkles of MLG due to defect is observed in the SEM image (see Fig. 6.1b).

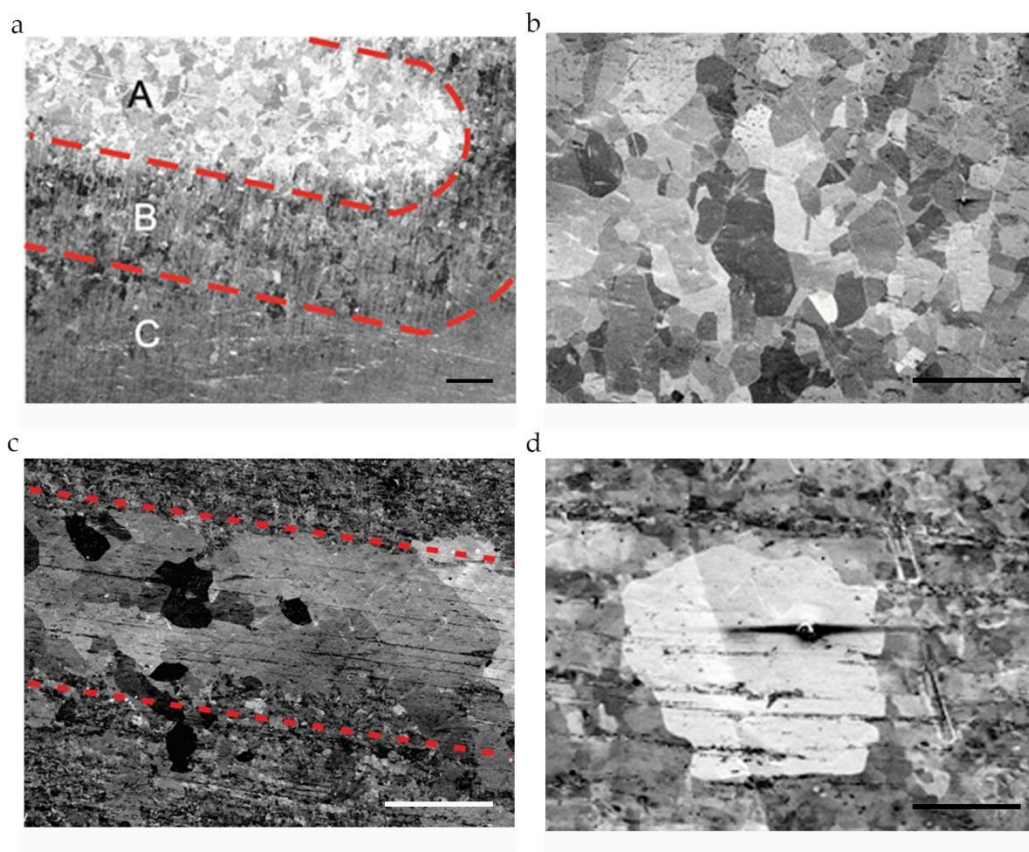


Figure 6. 1. The SEM image of a) the laser pathway on Ni foil (the scale bar is 100 μm), b) inside the laser pathway on Ni foil (the scale bar is 100 μm), c) the laser pathway on Pt foil (the scale bar is 100 μm), and d) isolated single domain graphene on Pt foil (the scale bar is 10 μm).

We attempted to synthesize a line of MLG on Pt foil by using LCVD. We applied the recipe used for Ni foil. We utilized a 25 μm thick Pt foil as the substrate. The quality of MLG grown on this foil is the same as that on Ni foil. There is also amorphous carbon found on this sample. However,

based on the SEM image, the laser pathway on this Pt foil is around 200 μm (see Fig. 6.1c), which is smaller than that on Ni foil. This due to thermal diffusion on Pt is slower than that on Ni foil. Hence, the temperature is more localized on Pt foil. The MLG is clearly observed on Pt foil in the SEM image. The wrinkled sheets with bright contrast indicate the MLG. The isolated single domain graphene was also observed on Pt foil (see Fig 6.1d).

It is likely that Pt foil gives a better result than that of Ni foil regarding the localized synthesis. The laser pathway on Pt foil is more localized than that on Ni foil. More effort to tune growth parameters on this foil is required to obtain high-quality graphene.

6.2. Outlook

In future, it is worthwhile to reinvestigate the gas mixture dependence of graphene growth on Pt Foil by using this LCVD technique. Several optimization experiments like on Ni foil are interesting because the experiment on this foil was only done once. The characterization for strengthening the interpretation of the presence of graphene

The defects generated in graphene flakes can be reduced by annealing the sample at a particular temperature. It is expected that graphene will gain energy to heal the defects into perfect structure [107, 108]. Since the results of these experiments show a defective MLG, it is worthwhile to try annealing the sample after growing to heal the defect. It is also can be tried to shine the laser on the line of MLG after growing. The laser will generate the heat to heal the defects in graphene. However, determining the best temperature for healing the defects need to be studied further.

It is also valuable to transfer the resulted line of graphene from the metal substrate into other substrates, such as a SiO_2 substrate. The AFM technique cannot work for our sample since the sample is too wavy due to a localized thermal by the laser. The surface of the sample is not flat, so can disturb the AFM image. By transferring the resulted graphene on SiO_2 substrate examining the thickness of the line by means of AFM technique could be done. We can use this technique in future to observe the morphology of the sample and strengthen our interpretation that has been done based on SEM image.

When the recipe for growing a line of high quality of graphene is obtained, the next challenging part would be how to narrow down the line of graphene. It can be done by focusing the laser beam into as small as possible and adjust the laser power accordingly. The line enlargement due to thermal properties of the substrate should be taken into account in this attempt.

The LCVD graphene may become an alternative method to pattern graphene rapidly. So far, the study of LCVD graphene was done on Ni foil as the substrate. In this work, we already showed that LCVD also work for Pt foil. The weak interaction between graphene and Pt foil makes it

possible to transfer graphene without etching the foil [60]. This nondestructive transfer technique, together with LCVD graphene on Pt foil, may enable various applications, such as integrating graphene on devices.

Acknowledgement

Alhamdulillah rabbil alamin... I would like to express my deepest gratitude to God for having made everything possible and giving me the strength and courage to finish this thesis.

Many people involved in finalizing this thesis. They gave scientific, technical and personal helps to complete this work. Therefore, in this opportunity, I would like to thank to:

- Prof. Meike Stöhr as my supervisor I. My sincere gratitude to you for guiding and supporting me to finish this master project. Thank you for your detail corrections in scientific and English part of my thesis.
- Dr. Ron Tobey as my supervisor II. Thank you very much for providing me a chance to conduct my master project in your laser lab and for supporting me to finish this work.
- My daily supervisor, Nico Schmidt, who has been guiding me thoroughly until the end of the work. Thank you for your critical comments in our discussions about the project. Thank you also for your help during the project and writing the thesis.
- Prof. Petra Rudolf as the group leader of Surface and Thin Film research group. Thank you for your valuable inputs and suggestions for my project during the group meeting.
- Jos and Miki as the technicians in our lab. Thank you, Jos, for your help in building the LCVD chamber. For Miki, thank you for your give me a hand in measuring Raman spectra on other help regarding the lab.
- Foppe and Ronnie. Thanks for helping me through the laser-related works and laser heating simulation.
- Lam and Ali. Thank you so much. Both of you help me a lot in measuring SEM images of my samples. Ali, thanks a lot for your support.
- All members in Surfaces and Thin Films research group: Leonid, Tashfeen, Brian, Dario, Jun, Bay, Florian, Sumit, Jiquan, Regis, Foqia, Dany, and Hilda. Thank you for all supports and helps during my work at the lab. It was really nice to be part of this group. I really enjoyed our togetherness when group meeting, outing, cake time, etc.
- LPDP (Indonesia endowment fund for education). Thank you very much for the financial support during my master study in Groningen.
- Last but not least, I would also like to say thank you to my wife, Nisa, and my son, Akyas, for everything; you two are always supportive. Thanks to my parents and my sisters for supporting me and also to all of my friends in Groningen who have given me a good time during my life in Groningen. Didik and family, Adhyat and family, Fajar and family, Zainal and family, Guntur, Didin, and Shidiq. I am sure that there are a lot more people that I am not able to mention one by one. Thank you very much.

Bibliography

- [1] A. K. Geim, K. S. Novoselov, "The rise of graphene," *Nature Materials*, vol. 6, pp. 183 - 191 , 2007.
- [2] H. P. Boem, R. Setton, E. Stumpp, "Nomenclature and terminology of graphite intercalation compounds," *Pure Applied Chemistry*, vol. 66, pp. 1893-1901, 1994.
- [3] Prezhdoo, O.V., "Graphene: The ultimate surface material," *Surface Science*, vol. 605, p. 1607, 2011.
- [4] K. S. Novoselov, A.K. Geim, S.V. Morozov, D. Jiang, Y. Zhang, S.v. Dubonos, I.V. Grigorieva, A.A. Firsov, "Electric Field Effect in Atomically Thin Carbon Films," *Science*, vol. 306, p. 666, 2004.
- [5] "The Nobel prize in physics 2010," Nobel Media AB, 2014. [Online]. Available: https://www.nobelprize.org/nobel_prizes/physics/laureates/2010/. [Accessed 29 June 2017].
- [6] P. R. Wallace, "The band theory of graphite," *Physical Review* , vol. 71, pp. 622-634, 1947.
- [7] X. Wang, Y. Shi, "Fabrication techniques of graphene nanostructures," in *Nanofabrication and its Application in Renewable Energy*, Cambridge, Royal Society of Chemistry, 2014, p. 3.
- [8] E. H. Hwang, S. D. Sarma, "Acoustic phonon scattering limited carrier mobility in 2D extrinsic graphene," *Physical Review B*, vol. 77, p. 115449, 2008.
- [9] K. I. Bolotin, K. J. Sikes, Z. Jiang, M. Klima, G. Fudenberg, J. Hone, P. Kim, H.L. Stormer, "Ultrahigh electron mobility in suspended graphene," *Solid State Communication*, vol. 146, p. 351, 2008.
- [10] C. R. Dean, A. F. Young, I. Meric, C. Lee, L. Wang, S. Sorgenfrei, K. Watanabe, T. Taniguchi, P. Kim, K. L. Shepard and J. Hone, "Boron nitride substrates for high-quality graphene electronics," *Nature Nanotechnology*, vol. 5, p. 722, 2010.
- [11] C. Lee, X. Wei, J. W. Kysar, J. Hone, "Measurement of the elastic properties and intrinsic strength of monolayer graphene," *Science*, vol. 321, p. 385, 2008.
- [12] A. A. Balandin, S. Ghosh, W. Bao, I. Calizo, D. Teweldebrhan, F. Miao, C.N. Lau, "Superior thermal conductivity of single-layer graphene," *Nano Letters*, vol. 8, p. 902, 2008.
- [13] X. Li, Y. Zhu, W. Cai, M. Borysiak, B. Han, D. Chen, R. D. Piner, L. Colombo, R. S. Ruoff, "Transfer of large-area graphene films for high-performance transparent conductive electrodes," *Nano Letters*, vol. 9, p. 4359, 2009.
- [14] R. R. Nair, P. Blake, A. N. Grigorenko, K. S. Novoselov, T. J. Booth, T. Stauber, N. M. R. Peres, A. K. Geim, "Fine structure constant defines visual transparency of graphene," *Science*, vol. 320, p. 1308, 2008.
- [15] M. Batzill, "The surface science of graphene: metal interfaces, CVD synthesis, nanoribbons, chemical modifications, and defects," *Surface Science Reports*, vol. 67, pp. 83-115, 2012.
- [16] J. M. Tour, "Top-down versus bottom-up fabrication of graphene-based electronics," *Chemistry of Materials*, vol. 26, pp. 163-171, 2014.
- [17] Md. S. A. Bhuyan, Md. N. Uddin, Md. M. Islam, F. A. Biphasa, S. S. Hossain, "Synthesis of

-
- graphene," *International Nano Letters*, vol. 6, pp. 65-83, 2016.
- [18] Y. Hernandez, V. Nicolosi, M. Lotya, F. M. Blighe, Z. Sun, S. De, I. T. McGovern, B. Holland, M. Byrne, Y. K. Gun'Ko, J. J. Boland, P. Niraj, G. Duesberg, S. Khrisnamurthy, R. Goodhue, J. Hutchison, V. Scardaci, A. C. Ferrari, J. N. Coleman, "High-yield production of graphene by liquid-phase exfoliation of graphite," *Nature Nanotechnol*, vol. 3, p. 563–568, 2008.
- [19] N. Liu, F. Luo, H. Wu, Y. Liu, C. Zhang, J. Chen, "One-step ionic-liquid-assisted electrochemical synthesis of ionic-liquidfunctionalized graphene sheets directly from graphite," *Journal of Advanced Functional Materials*, vol. 18, pp. 1518- 1525, 2008.
- [20] X. Wang, H. You, F. Liu, M. Li, L. Wan, S. Li, Q. Li, Y. Xu, R. Tian, Z. Yu, D. Xiang, J. Cheng, "Large-scale synthesis of few-layered graphene using CVD," *Chemical Vapor Deposition*, vol. 15, p. 53–56, 2009.
- [21] W. Zhang, J. Cui, C. Tao, Y. Wu, Z. Li, L. Ma, Y. Wen, and G. Li, "A strategy for producing pure single-layer graphene sheets based on a confined self-assembly approach," *Angewandte Chemie International*, vol. 48, p. 5864 –5868, 2009.
- [22] S. Karmakar, N. V. Kulkarni, A. B. Nawale, N. P. Lalla, R. Mishra, V. G. Sathe, S. V. Bhoraskar, A. K. Das, "A novel approach towards selective bulk synthesis of few-layer graphenes in an electric arc," *Jornal of Physics D: Applied Physics*, vol. 42, p. 115201, 2009.
- [23] W. A. de Heer, C. Berger, X. Wu, P. N. First, E. H. Conrad, X. Li, T. Li, M. Sprinkle, J. Hass, M. L. Sadowski, M. Potemski, G. Martinez, "Epitaxial graphene," *Solid State Communications*, vol. 143, p. 92–100, 2007.
- [24] A. Hirsch, "Unzipping Carbon Nanotubes: A Peeling Method for the Formation of Graphene Nanoribbons," *Angewandte Chemie International*, vol. 48, p. 6594 – 6596, 2009.
- [25] C. D. Kim, B. K. Min, W. S. Jung, "Preparation of graphene sheets by the reduction of Carbon Monoxide," *Carbon*, vol. 47, pp. 1605-1612, 2009.
- [26] K. S Kim, Y. Zhao, H. Jang, S.Y. Lee, J. M. Kim, K. S. Kim, J. H. Ahn, P. Kim, J. Y. Choi, B. H. Hong, "Large-scale pattern growth of graphene films for stretchable transparent electrodes," *Nature*, vol. 457, pp. 706- 710, 2009.
- [27] X. Li, W. Cai, J. An, S. Kim, J. Nah, D. Ynag, R. Piner, A. Velamakanni, I. Jung, E. Tutuc, S.K. Banerjee, L. Colombo, R. S. Ruoff, "Large-area synthesis of high-quality and uniform graphene films on copper foils," *Science*, vol. 324, pp. 1312-1314, 2009.
- [28] J. Coraux, A. T. N'Diaye, C. Busse, T. Michely, "Structural coherency of graphene on Ir(111)," *Nano Letters*, vol. 8, pp. 565-670, 2008.
- [29] S. Y. Kwon, C. V. Ciobanu, V. Petrova, V. B. Shenoy, J. Bareno, V. Gambin, I. Petrov, S. Kodambaka, "Growth of Semiconducting Graphene on palladium," *Nano Letters*, vol. 9, pp. 3985-3990, 2009.
- [30] P. W. Sutter, J.I. Fledge, E. A. Sutter, "Epitaxial graphene on ruthenium," *Nature Materials*, vol. 7, pp. 406-411, 2008.
- [31] Y. Zhao, Q. Han, Z. Cheng, L. Jiang, L. Qu, "Integrated graphene systems by laser irradiation for advanced devices," *Nano Today*, vol. 12, pp. 14-30, 2017.
- [32] Z. Lin, X. Ye, J. Han, Q. Chen, P. Fan, H. Zhang, D. Xie, H. Zhu, M. Zhong, "Precise control of the number of layers of graphene by picosecond laser thinning," *Scientific Reports*, vol. 5, pp. 11662-1- 11662-7, 2015.
- [33] G. Kalita, L. Qi, Y. Namba, K. Wakita, M. Umeno, "Femtosecond laser induced micropatterning
-

-
- of graphene film," *Science Direct*, vol. 65, pp. 1569-1572, 2011.
- [34] Y. Zhang, L. Guo, S. Wei, Y. He, H. Xia, Q. Chen, H. Sun, F. Xiao, "Direct imprinting of microcircuits on graphene oxides film by femtosecond laser reduction," *Nano Today*, vol. 5, pp. 15-20, 2010.
- [35] J. B. Park, W. Xiong, Y. Gao, M. Qian, Z.Q. Xie, M. Mitchell, Y. S. Zhou, G. H. Han, L. Jiang, Y. F. Lu, "Fast growth of graphene patterns by laser direct writing," *Applied Physics Letters*, vol. 98, pp. 123109-1 -123109-3, 2011.
- [36] J. Jiang, Z. Lin, X. Ye, M. Zhong, T. Huang, H. Zhu, "Graphene synthesis by laser-assisted chemical vapor deposition on Ni plate and the effect of process parameters on uniform graphene growth," *Thin Solid Films*, vol. 556, pp. 206-210, 2014.
- [37] W. Xiong, W. Hou, L. Jiang, M. M. Samani, J. Park, X. He, Y. Gao, L. Fan, T. Baldacchini, J. F. Silvani, Y. Lu, "Laser-based micro/nanofabrication in one, two and three dimensions," *Frontiers of Optoelectronics*, vol. 8, pp. 351-378, 2015.
- [38] M. I. Katsnelson, *Graphene: Carbon in two dimensions*, New York : Cambridge University Press, 2012.
- [39] J. N. Fuchs, M. O. Goerbig, "Introduction to the physical properties of graphene," Department of Physics Broida Hall, University of California, Santa Barbara, CA, 2008. [Online]. Available: http://web.physics.ucsb.edu/~phys123B/w2015/pdf_CoursGraphene2008.pdf. [Accessed 1 June 2017].
- [40] A. H. Castro Neto, F. Guinea, N. M. R. Peres, K. S. Novoselov, A. K. Geim, "The electronic properties of graphene," *Review of Modern Physics*, vol. 81, pp. 109-161, 2009.
- [41] A. Varykhalov, J. S. Barriga, A. M. Shikin, C. Biswas, E. Vescovo, A. Rybkin, D. Marchenko, O. Rader, "Electronic and magnetic properties of quasifreestanding graphene on Ni," *Physical Review Letters*, vol. 101, pp. 157601-1 -157601-4, 2008.
- [42] P. Sutter, J. T. Sadowski, E. Sutter, "Graphene on Pt(111): growth and substrate interaction," *Physical review B*, vol. 80, pp. 245211-1 -245211-10, 2009.
- [43] J. C. Shelton, H. R. Patil, J. M. Blakely, "Equilibrium segregation of carbon to a nickel (111) surface: A surface phase transition," *Surface Science*, vol. 43, pp. 493-520, 1974.
- [44] Y. Gamo, A. Nagashima, M. Wakabayashi, M. Terai, C. Oshima, "Atomic structure of monolayer graphite formed on Ni(111)," *Surface Science*, vol. 374, pp. 61-64, 1997.
- [45] J. Lahiri, T. S. Miler, A. J. Ross, L. Adamska, I. I. Oleynik, M. Batzill, "Graphene growth and stability at nickel surfaces," *New Journal of Physics*, vol. 13, p. 025001, 2011.
- [46] J. Lahiri, Y. Lin, P. Bozkurt, I. I. Oleynik, M. Batzill, "An extended defect in graphene as a metallic wire," *Nature Nanotechnology*, vol. 5, pp. 326-329, 2010.
- [47] A. Nagashima, N. Tejima, and C. Oshima, "Electronic states of the pristine and alkali-metal-intercalated monolayer graphite/Ni(111) systems," *Physical Review B*, vol. 50, pp. 1787-17495, 1994.
- [48] Y. S. Dedkov, M. Fonin, U. Rudiger, C. Laubschat, "Rashba effect in the graphene/Ni(111) system," *Physical Review Letters*, vol. 100, pp. 107602-1 -107602-4, 2008.
- [49] P. Merino, M. Svec, A. L. Pinardi, G. Otero, J. A. Martin-Gago, "Strain-driven Moire superstructures of epitaxial graphene on transition metal surfaces," *American Chemical Society Nano*, vol. 5, pp. 5627-5634, 2011.
- [50] G. Giovannetti, P. A. Khomyakov, G. Brocks, V. M. Karpan, J. van den Brink, P. J. Kelly, "Doping graphene with metal contacts," *Physical Review Letters*, vol. 101, pp. 026803-1 -
-

026803-4, 2008.

- [51] A. Jorio, R Saito, G. Dresselhaus, and M S. Dresselhaus, Raman spectroscopy in graphene related system, Weinheim: Wiley-VCH Verlag GmbH & Co. KGaA, 2011.
- [52] A. C. Ferrari , D. M. Basko, "Raman spectroscopy as a versatile tool for studying the properties of graphene," *Nature Nanotechnology*, vol. 8, pp. 235-246, 2013.
- [53] P. Atkins, J. de Paula, Physical chemistry 9th edition, New York: W.H. Freeman and Company, 2010.
- [54] J. Hodkiewicz, "Characterizing graphene with Raman spectroscopy," *Thermo Fisher Scientific*, 2011.
- [55] R. Reichelt, "Scanning electron microscopy," in *Science of microscopy*, New York, Springer, 2007, pp. 133-135.
- [56] R. F. Egerton, Physical principles of electron microscopy: An introduction to TEM, SEM, and AEM, New York: Springer, 2005.
- [57] P. Echlin, Handbook of sample preparation for scanning electron microscopy and X-ray microanalysis, New York: Springer, 2009.
- [58] S. Bradbury, B. J. Ford, D. C. Joy, "Encyclopedia Britannica: Scanning electron microscope (SEM)," [Online]. Available: <https://www.britannica.com/technology/scanning-electron-microscope>. [Accessed 16 June 2017].
- [59] L. Huang, Q. H. Chang, G. L. Guo, Y. Liu, Y. Q. Xie, T. Wang, B. Ling, H. F. Yang, "Synthesis of high-quality graphene films on nickel foils by rapid thermal chemical vapor deposition," *Carbon*, vol. 50, pp. 551- 556, 2012.
- [60] L. Gao, W. Ren, H. Xu, L. Jin, Z. Wang, T. Ma, L. Ma, Z. Zhang, Q. Fu, L. Peng, X. Bao, H. Cheng, "Repeated growth and bubbling transfer of graphene with millimetre-size single-crystal grains using platinum," *Nature Communications*, vol. 3, pp. 699-1- 699-7, 2012.
- [61] J. I. Goldstein, Practical scanning electron microscopy, New York : 1975, 1975.
- [62] S. J. Chae, F. Gunes, K. K. Kim, E. S. Kim, G. H. Han, S. M. Kim, H. Shin, S. Yoon, J. Choi, M. H. Park, C. W. Yang, D. Pribat, Y. H. Lee, "Synthesis of large-area graphene layers on polynickel substrate by chemical vapor deposition: Wrinkle formation," *Advanced Materials*, vol. 21, pp. 2328- 2333, 2009.
- [63] H. Pierson, Handbook of chemical vapor deposition 2nd edition, New Jersey: Noyes Publications, 1999.
- [64] Y. Zhang, L. Zhang, C. Zhou, "Review of chemical vapor deposition of graphene and realated application," *Accounts of Chemical Research*, pp. 2329-2339, 2013.
- [65] Q. Yu, J. Lian, S. Siriponglert, H. Li, Y. P. Chen, S. Pei, "Graphene segregated on Ni surfaces and transferred to insulators," *Applied Physics Letters*, vol. 93, pp. 113103-1- 113103-3, 2008.
- [66] A. Reina, X. Jia, J. Ho, D. Nezich, H. Son, V. Bulovic, M. S. Dresselhaus, J. Kong, "Large area, few-layer graphene films on arbitratry substrate by chemical vapor deposition," *Nano Letters*, vol. 9, pp. 30- 35, 2009.
- [67] X. Li, W. Cai, J. An, S. Kim, J. Nah, D. Yang, R. Piner, A. Velamakanni, I. Jung, E. Tutuc, S. K. Banarjee, L. Colombo, R. S. Ruoff, "Large-area synthesis of high-quality and uniform graphene films on copper foils," *Science*, vol. 324, pp. 1312-1314, 2009.
- [68] C. Mattevi, H. Kim, M. Chhowalla, "A review of chemical vapor deposition of graphene on copper," *Journal of Materials Chemistry*, pp. 3324-3334, 2010.
- [69] M. Losurdo, M. M. Giangregorio, P. Capezzuto, G. Bruno, "Graphene CVD growth on copper

-
- and nickel: role of hydrogen in kinetics and structure," *Physical Chemistry Chemical Physics*, vol. 13, p. 20836–20843, 2011.
- [70] A. Dahal, M. Batzill, "Graphene-nickel interfaces: a review," *Nanoscale*, vol. 6, p. 2548–2562, 2014.
- [71] R. S. Weatherup, A. J. Shahani, Z. Wang, K. Mingard, A. J. Pollard, M. Willinger, R. Schloegl, P. W. Voorhees, S. Hofmann, "In situ graphene growth dynamics on polycrystalline catalyst foils," *Nano Letters*, vol. 16, pp. 6196–6206, 2016.
- [72] J. Sun, Y. Nam, N. Lindvall, M. T. Cole, K. B. K. Teo, Y. W. Park, A. Yurgens, "Growth mechanism of graphene on platinum: Surface catalysis and carbon segregation," *Applied Physics Letters*, vol. 104, pp. 152107-1–152107-4, 2014.
- [73] L. M. Harwood, C. J. Moody, J. M. Percy, *Experimental organic chemistry: standard and microscale*, WileyBlackw, 1989.
- [74] H. Zhou, W. J. Yu, L. Liu, R. Cheng, Y. Chen, X. Huang, Y. Liu, Y. Wang, Y. Huang, X. Duan, "Chemical vapor deposition growth of large single crystals of monolayer and bilayer graphene," *Nature Communications*, vol. 4:2096, pp. 1–8, 2013.
- [75] D. Jean, W. J. Lackey, C. E. Duty, "Temperature controlled laser chemical vapor deposition (LCVD) using thermal imaging," *Assembly Automation*, vol. 25, pp. 293–299, 2005.
- [76] D. Bauerle, *Laser processing and chemistry*, New York: Springer, 2011.
- [77] S. N. Bondi, W. J. Lackey, R. W. Johnson, X. Wang, Z. L. Wang, "Laser assisted chemical vapor deposition synthesis of carbon nanotubes and their characterization," *Carbon* 44, pp. 1393–1403, 2006.
- [78] J. Lackey, D. Rosen, C. Duty, D. Jean, S. Bondi, T. Elkhatib, R. Johnson, M. Jiang, J. Mi, J. Gillespie, R. Harvey, "Laser CVD system design, operation, and modeling," in *26th Annual conference on composites, advanced ceramics, materials, and structures: B: ceramic engineering and science proceedings*, The American Ceramic Society, 2008, pp. 23–33.
- [79] A. C. Ferrari, J. Robertson, "Raman spectroscopy of amorphous, nanostructured, diamond-like carbon, and nanodiamond," *Philosophical transactions of The Royal Society A*, vol. 362, pp. 2477–2512, 2004.
- [80] J. R. Durig, J. S. Church, C. M. Whang, R. D. Johnson, B. J. Streusand, "Spectra and structure of organophosphorus compounds. infrared and Raman spectra, conformational stability, barriers to internal rotation, vibrational assignment, and normal coordinate analysis of ethyldifluorophosphine," *The Journal of Physical Chemistry*, vol. 91, pp. 2769–2778, 1987.
- [81] K. Virkler, I. K. Lednev, "Raman spectroscopy offers great potential for the nondestructive confirmatory identification of body fluids," *Forensic Science International*, vol. 181, p. e1–e5, 2008.
- [82] P. Reinke, W. Jacob, W. Müller, "Influence of the ion energy on the growth and structure of thin hydrocarbon films," *Journal of Applied Physics*, vol. 74, pp. 1354–1361, 1993.
- [83] A. Kaniyoor, S. Ramaprabhu, "A Raman spectroscopic investigation of graphite oxide derived graphene," *American Institute of Physics*, vol. 2, pp. 032183-1–032183-12, 2012.
- [84] P. K. Chu, L. Li, "Characterization of amorphous and nanocrystalline carbon films," *Materials Chemistry and Physics*, vol. 96, p. 253–277, 2006.
- [85] C. Luo, D. Li, W. Wu, Y. Zhang, C. Pan, "Preparation of porous micro–nano-structure NiO/ZnO heterojunction and its photocatalytic property," *Royal Society of Chemistry Advances*, vol. 4, pp. 3090–3095, 2014.
-

-
- [86] X. Su, H. Chai, D. Jia, S. Bao, W. Zhou, M. Zhou, "Effective microwave-assisted synthesis of graphene nanosheets/NiO composite for high-performance supercapacitors," *Royal Society of Chemistry*, vol. 37, pp. 439-443, 2013.
- [87] N. M. Ulmane, A. Kuzmin, I. Sildos, M. Pars, "Polarisation dependent Raman study of single-crystal nickel oxide," *Central European Journal of Physics*, vol. 9(4), pp. 1096- 1099, 2011.
- [88] B. Zhao, J. Song, P. Liu, W. Xu, T. Fang, Z. Jiao, H. Zhang, Y. Jiang, "Monolayer graphene/NiO nanosheets with two-dimension structure for supercapacitor," *Journal of Materials Chemistry*, vol. 21, p. 18792–18798 This, 2011.
- [89] "Raman spectroscopy in more detail," [Online]. Available: <http://www.renishaw.com/en/raman-spectroscopy-in-more-detail-25806>. [Accessed 2017 July 3].
- [90] "Melting temperatures of some common metals and alloys," [Online]. Available: http://www.engineeringtoolbox.com/melting-temperature-metals-d_860.html. [Accessed 3 July 2017].
- [91] M. A. Al-Nimr, "Heat transfer mechanism during short-duration laser heating on thin metal films," *International Journal of Thermophysics*, vol. 18, pp. 1257- 1268, 1997.
- [92] P. Patnaik, Handbook of inorganic chemicals, New York: McGraw-Hill Publications, 2003.
- [93] R. Alizadeh, E. Jamshidi, H. Ale-Ebrahim, "Kinetic study of nickel oxide reduction by methane," *Chemical Engineering & Technology*, vol. 30, pp. 1123- 1128, 2007.
- [94] H. Rashidi, H. Ale Ebrahim, B. Dabir, "Reduction kinetics of nickel oxide by methane as reducing agent based on thermogravimetry," *Thermochimica Acta*, vol. 561, pp. 41- 48, 2013.
- [95] P. Danielson, "Source of water vapor in vacuum systems," [Online]. Available: <http://www.normandale.edu/departments/stem-and-education/vacuum-and-thin-film-technology/vacuum-lab/articles/sources-of-water-vapor-in-vacuum-systems>. [Accessed 2 July 2017].
- [96] P. Danielson, "Pumping water vapor," [Online]. Available: <http://www.normandale.edu/departments/stem-and-education/vacuum-and-thin-film-technology/vacuum-lab/articles/pumping-water-vapor>. [Accessed 5 July 2017].
- [97] J. M. Blakeley, J. S. Kim, H. C. Potter, "Segregation of carbon to the (100) surface of nickel," *Journal of Applied Physics*, vol. 41, pp. 2693- 2697, 1970.
- [98] A.C. Ferrari, D.M. Basko, "Raman spectroscopy as a versatile tool for studying the properties of graphene," *Nature Nanotechnology*, vol. 8, pp. 235-246, 2013.
- [99] J. Hodkiewicz, "Characterizing graphene with raman spectroscopy," *Thermo Fisher Scientific*, 2011.
- [100] E. H. M. Ferreira, M. V. O. Moutinho, F. Stavale, M. M. Lucchese, R. B. Capaz, C. A. Achete, A. Jorio, "Evolution of the Raman spectra from single-, few-, and many-layer graphene with increasing disorder," *Physical Review B*, vol. 82, pp. 125429-1- 125429-9, 2010.
- [101] R. E. Shroder, R. J. Nemanich, J. T. Glass, "Analysis of the composite structures in diamond thin films by Raman spectroscopy," *Physical Review B*, vol. 41, pp. 3738-3745, 1990.
- [102] P. Milani, M. Ferretti, P. Piseri, C. E. Bottani, A. Ferrari, A. Li Bassi, G. Guizzetti, M. Patrini, "Synthesis and characterization of cluster-assembled carbon thin films," *Journal of Applied Physics*, vol. 82, pp. 5793-5798, 1997.
- [103] L. Baraton, Z. B. He, C. S. Lee, C. S. Cojocaru, M. Chatelet, J. L. Maurice, Y. H. Lee, D. Pribat, "On the mechanisms of precipitation of graphene on nickel thin films," *Europhysics Letters*, vol. 96, pp. 46003-1- 46003-6, 2011.
-

-
- [104] J. Xie, J. P. Spallas, "Different contrast mechanisms in SEM imaging of graphene," [Online]. Available: <http://www.toyo.co.jp/files/user/img/product/microscopy/pdf/5991-0782EN.pdf>. [Accessed 2 July 2017].
- [105] K. H. Kim, Z. Akase, T. Suzuki, D. Shindo, "Charging effects on SEM/ SIM contrast of metal/ insulator system in various metallic coating conditions," *Materials Transactions*, vol. 51, pp. 1080- 1083, 2010.
- [106] "Thermal conductivity: platinum," [Online]. Available: http://www.efunda.com/materials/elements/TC_Table.cfm?Element_ID=Pt. [Accessed 5 July 2017].
- [107] J. Chen, T. Shi, T. Cai, T. Xu, L. Sun, "Self healing of defected graphene," *Applied Physics Letters*, vol. 102, pp. 103107- 103107-5, 2013.
- [108] M. Zheng, K. Takei, B. Hsia, H. Fang, X. Zhang, N. Ferralis, H. Ko, Y. Chueh, Y. Zhang, R. Maboudian, A. Javey, "Metal-catalyzed crystallization of amorphous carbon to graphene," *Applied Physics Letters*, vol. 96, pp. 063110-1- 063110-3, 2010.